BBA - General Subjects 1864 (2020) 129466

Contents lists available at ScienceDirect

BBA - General Subjects

journal homepage: www.elsevier.com/locate/bbagen

Time-resolved studies of metalloproteins using X-ray free electron laser radiation at SACLA

Michihiro Suga[a,*], Atsuhiro Shimada[b,*], Fusamichi Akita[a], Jian-Ren Shen[a], Takehiko Tosha[c], Hiroshi Sugimoto[c,*]

[a] Research Institute for Interdisciplinary Science and Graduate School of Natural Science and Technology, Okayama University, 3-1-1 Tsushima Naka, Okayama 700-8530, Japan.
[b] Graduate School of Applied Biological Sciences and Faculty of Applied Biological Sciences, Gifu University, 1-1 Yanagido, Gifu 501-1193, Japan.
[c] Synchrotron Radiation Life Science Instrumentation Team, RIKEN SPring-8 Center, 1-1-1 Kouto, Sayo, Hyogo 679-5148, Japan.

ARTICLE INFO

Keywords:
X-ray free-electron laser
Serial femtosecond crystallography
Heme
Metalloproteins
Radiation damage
Proton pump

ABSTRACT

Background: The invention of the X-ray free-electron laser (XFEL) has provided unprecedented new opportunities for structural biology. The advantage of XFEL is an intense pulse of X-rays and a very short pulse duration (< 10 fs) promising a damage-free and time-resolved crystallography approach.
Scope of review: Recent time-resolved crystallographic analyses in XFEL facility SACLA are reviewed. Specifically, metalloproteins involved in the essential reactions of bioenergy conversion including photosystem II, cytochrome *c* oxidase and nitric oxide reductase are described.
Major conclusions: XFEL with pump-probe techniques successfully visualized the process of the reaction and the dynamics of a protein. Since the active center of metalloproteins is very sensitive to the X-ray radiation, damage-free structures obtained by XFEL are essential to draw mechanistic conclusions. Methods and tools for sample delivery and reaction initiation are key for successful measurement of the time-resolved data.
General significance: XFEL is at the center of approaches to gain insight into complex mechanism of structural dynamics and the reactions catalyzed by biological macromolecules. Further development has been carried out to expand the application of time-resolved X-ray crystallography. This article is part of a Special Issue entitled Novel measurement techniques for visualizing 'live' protein molecules.

1. Introduction

X-ray crystallography using synchrotron radiation is currently the most powerful method in determining high-resolution structures of biological macromolecules. However, a major problem in conventional synchrotron-based X-ray crystallography is radiation damage, since the ionizing effects of the X-ray beam changes the structure of the protein [1,2]. X-ray irradiation produces both global and specific radiation damage to the crystal of biological macromolecules, even at cryo-temperatures [1,2]. Global damage of crystals appears as a gradual fading of the intensities of Bragg reflection spot and vanishing of weak high-angle reflections [3]. In addition to these visually apparent changes, processed data also shows increased unit cell dimensions, crystal mosaicity and Wilson *B*-factors, as well as worse data statistics overall (*eg.* $I/\sigma(I)$, $CC_{1/2}$ and *R*-merge). There are also specific chemical changes that can be seen mainly by the reduction of transition metals, disulfide bond breakage or elongation and decarboxylation of acidic amino acid residues. Specific damage is faster than global damage [4].

The presence of large numbers of high energy solvated electrons generated by X-ray irradiation during diffraction data collection is of particular impact for studies on redox-sensitive systems such as metalloproteins [5,6]. Metal cofactors can absorb free electrons and change their oxidation states, which can affect their coordination structure of ligands. These specific radiation damages involving metal ions in the active site can be misleading in the studies of the reaction intermediates. In such cases, special care is required when building the model in the electron density and interpreting crystal structures that have been modified by X-ray damage during the data collection. However, separating the radiation damage from an enzymatic reaction mechanism and drawing the valid biological conclusions from crystal structures can be extremely difficult.

Many efforts have been reported to obtain more intact protein structures using X-rays from synchrotron and neutron scattering [7–10]. In contrast, a recently emerged serial femtosecond

* Corresponding author.
E-mail addresses: michisuga@okayama-u.ac.jp (M. Suga), ashima@gifu-u.ac.jp (A. Shimada), sugimoto@spring8.or.jp (H. Sugimoto).

https://doi.org/10.1016/j.bbagen.2019.129466
Received 20 June 2019; Received in revised form 2 October 2019; Accepted 4 October 2019
Available online 31 October 2019

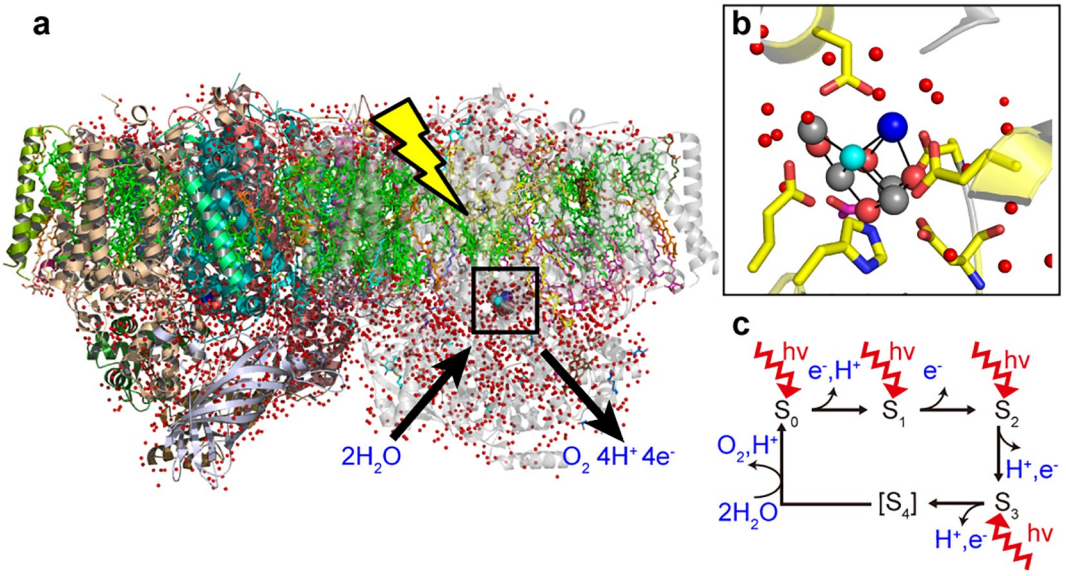

Fig. 1. Structure of PSII and water oxidation reaction. **(a)** Crystal structure of PSII. **(b)** Structure of the OEC and its ligand environment. **(c)** The Kok-cycle.

crystallography (SFX) approach using X-ray Free Electron Laser (XFEL) source overcomes radiation damage. The intense XFEL pulse results in the complete destruction of any exposed microcrystal, yet the pulses are so short that the diffraction from the crystal sample by a single XFEL pulse occurs before the onset of significant radiation damage [11–13]. This scheme of "diffraction before destruction" [14] requires a fresh crystal to be delivered to the XFEL beam position for the next pulse [15,16]. Intense XFEL pulses enable the determination of high-resolution structures of proteins from a very small crystal size as well as for extremely radiation sensitive macromolecules, such as metalloenzymes, without any radiation damage. As another advantage for the use of XFEL, the short duration of XFEL pulses allow access to dynamic information about unstable intermediate states, opening a new era of time-resolved structural studies [13,17,18].

In addition to the damage-free structures obtained by XFEL experiments, the information of the location of individual hydrogen atoms and the protonation states of catalytically important residues provides important insight into catalytic processes of proteins. Neutron diffraction is a complementary technique because it is uniquely able to visualize hydrogen atoms in structures at moderate resolutions (< 2.5 Å) [19]. Neutrons can be used as gentle non-ionizing probes that easily penetrate fragile biological samples without causing radiation damage, because they are uncharged and have low thermal energies (0.1–10 meV) [20]. X-ray and neutron diffraction datasets can be combined for crystallographic structure refinement, but a major limitation is that the flux of available neutron beams (10^6–10^8 neutrons $cm^{-2}\,s^{-1}$) is many orders of magnitude less than beams from conventional X-ray generators, requiring larger crystals and very long exposure times to have detectable diffraction signals [20].

This review describes the XFEL-based crystallographic studies, especially time-resolved X-ray crystallography, on three metalloproteins performed at SACLA, an XFEL facility in Japan [21]. The first example is on photosystem II (PSII) in which photo-illumination initiates the O_2 evolution reaction [22,23]. In the second example, the structural dynamics of cytochrome *c* oxidase (CcO) [24] are described. In this case, a photolabile ligand is utilized as a trigger for time-resolved crystallography. In the final example an attempt to observe the catalytic reaction of nitric oxide (NO) reductase cytochrome P450 (P450nor) using a photosensitive caged substrate is explained [25]. In addition, insights into the future of time-resolved crystallography using XFELs are also discussed.

2. Photosystem II

2.1. Introduction of photosystem II

Plants and other oxygenic photosynthetic organisms synthesize carbohydrates from water molecules and carbon dioxide in the atmosphere by utilizing light energy from the sun and concurrently releasing dioxygen molecules as a byproduct. This process is called photosynthesis, which is achieved by a chain of electrons, a series of proton transfers and enzymatic reactions cooperatively catalyzed by many proteins. The first reaction of photosynthesis is the water oxidation by PSII, a huge membrane protein complex consisting of 20 protein subunits. PSII utilizes light energy to oxidize water to dioxygen with the removal of four protons and electrons according to the following equation.

$$2H_2O \rightarrow 4H^+ + 4e^- + O_2$$

This water splitting and oxygen evolving reaction is catalyzed at the catalytic center of PSII, termed the oxygen evolving complex (OEC), through five oxidation steps of the Kok cycle (S_i-state cycle, $i = 0$–4), where the S_4 state is the most oxidized transient state that releases dioxygen and successively turns back to the S_0 state [26]. During the reaction cycle, the OEC is known to change its structure slightly to control the reaction precisely. In addition to an enormous amount of progress in X-ray spectroscopy and electron paramagnetic resonance studies [27–30], X-ray structure of PSII in the S_1 state under dark adaptation condition showed that the OEC has a chemical composition of the Mn_4CaO_5 cluster as shown in Fig. 1 [31]. The structure uncovered all oxo-bridges of the OEC and the hydrogen bonding network of the amino acids and water molecules surrounding it. This solid structural basis greatly advanced our understanding of the reaction mechanism in combination with theoretical calculations and spectroscopic methods [32,33]. However, two critical issues remained unresolved: First, irradiation by strong X-rays of synchrotron radiation (SR) during data collection may damage the OEC. Second, the crystal structures in the intermediate S_i-states were not solved but are indispensable for elucidating the full mechanism of water splitting. XFEL-based crystallographic techniques such as damage-free structural analysis and time-resolved crystallography enabled us to overcome these essential issues [14]. Here, we review how XFEL is contributing to the structural studies of PSII.

2.2. Radiation damage free structure of PSII in the S_1 state

In the Mn_4CaO_5 cluster of the OEC, three Mn atoms and one Ca atom form the Mn_3CaO_4 cuboid cluster and the fourth Mn atom is connected at the outside of the cuboid by two oxo-bridges, making the whole structure resembling a distorted chair [31] (Fig. 1). Two distinguishable features of this natural catalyst compared to the artificial inorganic catalysts are as follows: One is the difference in the bond distance between Ca and oxygen and the typical bond distances between Mn and oxygen, with the former (2.3–2.5 Å) slightly longer than the latter (1.8–2.1 Å), making the Mn_3CaO_4 cuboid asymmetric. The other is the differences among the bond distances of Mn-oxygen atoms, where O5, an oxo-bridge connecting the cuboid and the fourth Mn atom has longer distances with its nearby Mn atoms (2.4–2.7 Å) than the typical Mn-oxygen distances. The longer bond distances suggest that O5 binds weakly to the Mn atoms, and therefore it may serve as one of the substrates for the dioxygen formation. The Mn−Mn distances determined in the SR structure of the OEC, however, are slightly longer (0.1–0.2 Å) than those obtained by extended X-ray absorption fine structures (EXAFS) [34,35] or theoretical calculations based on the SR structure [36–38]. These discrepancies were likely brought by the specific radiation damage mentioned above during data collection. Indeed, EXAFS showed the possibility that the X-ray dose used for the SR analysis reduced 25% of the OEC Mn atoms to Mn^{2+} atoms [39]. In fact, the three shortest Mn−Mn distances of the 1.9-Å resolution structure (PDB 3WU2) are 2.8 Å, 2.9 Å and 3.0 Å [22], whereas the corresponding values by the EXAFS are 2.7 Å, 2.7 Å and 2.8 Å, respectively [30]. While the inconsistencies between them were similar to the estimated errors in the X-ray structure (the Cruickshank diffraction-component precision index (DPI) [40] is 0.11 Å), clarification of the slight differences found in the Mn−Mn distances between the SR structure and EXAFS/theoretical studies may be necessary for the elucidation of the reaction mechanism. This is because catalysts usually change and arrange their structures slightly during the catalytic cycles, and the OEC may change its structure to a similar extent during the Kok cycle [41]. In order to eliminate the possible effects of radiation damage, diffraction data was collected using femtosecond XFEL pulses and the structure at 1.95 Å resolution was analyzed to distinguish slight differences in the bond lengths from the coordinate error or radiation damage [22]. Since PSII is a large membrane protein complex with a molecular mass of about 700-kDa in a dimeric form, PSII crystals in large sizes, with a maximum length of 1 mm were used with a fixed-target serial femtosecond rotational crystallography (SF-ROX) approach [42]. SF-ROX is one of the data collection methods compatible with the “diffraction-before-destruction” paradigm of XFEL crystallography [14]. The irradiation points by the XFEL pulses were separated by 50 μm on the large PSII crystals and it was confirmed that this distance is enough to ensure that every irradiation point on the crystal was not damaged. A few hundred of highly isomorphous, large PSII crystals were used to collect a full dataset and two independent datasets were obtained from two different preparations of the crystals and the structure at 1.95 Å resolution was analyzed from both datasets to determine the interatomic distances based on the average of two structures (PDB 4UB6 and 4UB8). The OEC was independently determined in two non-crystallographic symmetry related PSII monomers, giving some indication of the agreement of OEC across monomers and across datasets.

The overall structure of the OEC determined by using XFEL is similar to the SR structure. The orientation of the side chains, except for in the vicinity of metal-binding sites, as well as most of the water molecules found in each structure, are almost identical, indicating that X-ray diffraction is sufficient to determine the overall protein environment. However, differences are found in the interatomic distances of the Mn atoms as shown in Fig. 2. Notably, all the interatomic distances between the Mn atoms are shorter by 0.1–0.2 Å compared with the SR structure, and they are mostly consistent with the results of EXAFS. This suggests that the XFEL structure is radiation-damage free and the previous SR structure may have suffered some radiation damage, leading to partial reductions of the Mn atoms and therefore causing slight elongations of the distances between the Mn atoms.

The exceptionally longer distances between O5 and Mn atoms (Mn1, Mn3, and Mn4) found in the SR structure have provoked discussions on the possible role of the O5 atom in the water splitting reaction. In the XFEL structure, the bond distances between the metal atoms and O5 are 2.7 Å (Mn1-O5), 2.2 Å (Mn3-O5), 2.3 Å (Mn4-O5), and 2.5 Å (Ca-O5), respectively. Thus, the feature of long bond distances between O5 and the Mn atoms remained, although the bond of Mn1-O5 is longer by 0.1 Å and the other bonds Mn3-O5, Mn4-O5 and Ca-O5 are shorter by 0.1 Å than those of the SR structure. This suggests that the feature of the long bond distances between Mn and O5 is not an artifact of radiation damage, but an inherent characteristic of the catalyst. Based on the Mn−O and Mn-ligand distances revealed by the radiation-damage free structure as well as the existence of a Jahn-Teller axis on the Mn^{+3} atoms, the valances of the four Mn atoms are consistent with a distribution of (Mn1, Mn2, Mn3, Mn4) = (+3, +4, +4, +3) in the S_1 state [27,43]. The high resolution, XFEL structure obtained provides a vital understanding of the relationship between the structure of the OEC and its physical properties.

2.3. Structure of PSII in the intermediate S_3 state

Although the XFEL structural analysis of PSII in the S_1 state revealed the accurate interatomic distances of the OEC and the putative valance states of the four Mn atoms, detailed structural changes that occur during the reaction cycle remained unknown. In particular, the long bond distances between O5 and Mn atoms suggested that its binding is weak and unstable, and therefore the O═O bond formation may proceed between the O5 atom and a water molecule newly inserted in the intermediate S_i-state. This reaction mechanism has indeed been discussed based on the results of theoretical calculations, spectroscopies and crystal structures by SR and XFEL, however, the reaction mechanism cannot be determined from the structure in the S_1 state only, and other types of mechanisms have also been proposed and discussed [44,45]. In order to reveal the real mechanism of water oxidation, structural analysis of the intermediate S_i-states are indispensable. Especially, the highest metastable intermediate S_3 state was considered to be important because spectroscopy showed that all Mn atoms of the OEC become octahedrally coordinated in S_3 while one of the Mn atoms in S_2 is five coordinated, suggesting an insertion and binding of the possible substrate water into the OEC during the S_2 to S_3 transition [27]. There have been several reports on the structural analysis of intermediate S_i-states using the approach of pump-probe with the XFEL-SFX method [46–48], which demonstrated simultaneous crystallography and spectroscopy measurement at an XFEL, showing that the Mn ions are not affected by the intense XFEL pulses [37,39]; however, these works were not conclusive for the O═O bond formation mechanism due to the insufficient resolution of the diffraction data. For example, insertion of a new water during the S_i-state transitions was not observed, and it was not clear how and where protons were released from the OEC, with regards also to the mechanism that prevents backflow of protons. To answer these questions, the structure of PSII in the intermediate S_3 state was analyzed.

Light energy transferred to the reaction center of PSII (P680) initiates the initial charge separation between P680 and pheophytin, and consequently an electron is transferred to plastquinone QB through the electron transport chain, thereby generating a proton gradient across the thylakoid membrane and reducing equivalents for CO_2 assimilation. The positive charge on $P680^+$ generated immediately oxidizes the radical active tyrosine YZ (Try-161), which then oxidizes the OEC. Until accumulation of the four oxidizing equivalents (S_4 state), each step of the S_i-state transitions in the Kok-cycle is driven by the absorption of one photon at P680, causing structural changes on the order of tens of microseconds to a few milliseconds. The O═O bond formation and

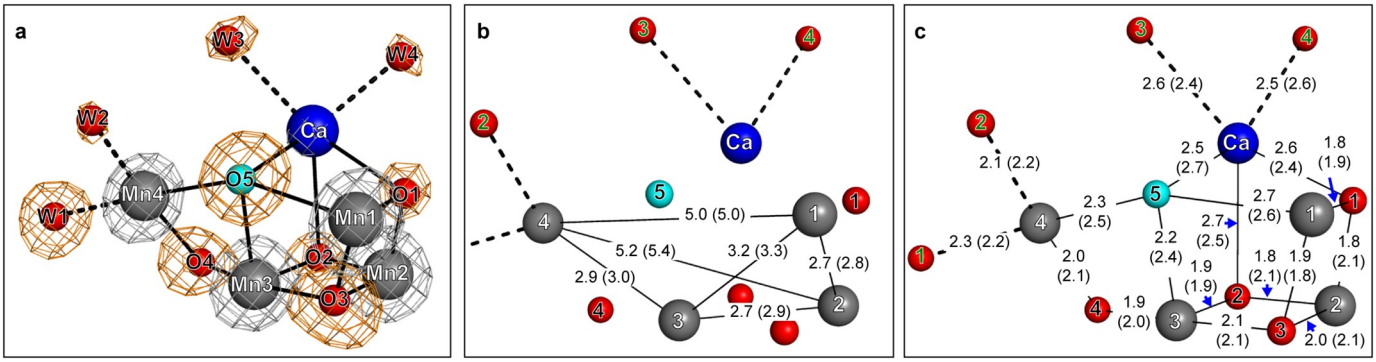

Fig. 2. Radiation damage free structure of PSII in the S_1 state determined by the SF-ROX method. **(a)** Structure of the Mn_4CaO5 cluster shown with electron density maps of individual atoms. The $2mF_o$-DF_c map and the oxygen-omit mF_o-DF_c map are shown as gray and brown meshes and contoured at 7 σ and 6 σ levels, respectively. **(b, c)** Interatomic distances (Å) between Mn atoms **(b)** and Mn—O and Ca—O **(c)**. Numbers in bracket indicate the corresponding distances in the SR structure.

release of the dioxygen molecule occur during the transitions of $S_3 \rightarrow (S_4) \rightarrow S_0$ as mentioned above (Fig. 1C). PSII microcrystals with a maximum length of 100 μm were prepared to ensure both high efficiencies of excitation for the advancement of the Kok-cycle [49] and a high resolution of the diffraction by the method of SFX. The PSII crystals were excited by two laser flashes separated by 10 ms to advance the dark-adapted S_1 state to the S_3 state, followed by exposure to the XFEL pulses 10 ms after the second flash. The structures of the dark-adapted S_1 state and the doubly flashed S_3 dominant state were analyzed at 2.35 Å resolution [23].

The overall structure of PSII in the S_3 state is almost identical to the S_1 state structure. The difference Fourier map between the isomorphous datasets is most potent to detect subtle structural changes in the time-resolved analysis, where structural changes induced by the transition to the different state appear as positive densities while the structure that is not identical to the initial state appears as negative densities. Thus, a high isomorphism between the datasets is critical for the difference Fourier map to yield meaningful signals. The F_{obs} (S_3) - F_{obs} (dark) difference Fourier map obtained showed pairs of positive and negative peaks covering the regions around the OEC and QB as shown in Fig. 3, indicating the occurrence of light-induced structural changes at both electron acceptor and donor sides. This indicates efficient progress of the Kok cycle within the crystals.

The difference Fourier map revealed that six significant structural changes occurred around the OEC during the progress of the Kok-cycle (Fig. 4). They are: (i) The Mn4 atom moves slightly outward from the OEC, and consequently, the interatomic distance between Mn4 and Mn1 becomes longer by 0.1–0.2 Å. (ii) The Ca atom of the OEC moves slightly away from Mn4. (iii) A sharp electron density which corresponds to a new water molecule O6 appears at a position near O5. (iv) The side chain of E189 flips away from the OEC providing a space that can accommodate the O6 between Mn1 and O5. (v) A strong negative electron density covering the water 665 (W665) was observed, suggesting that W665 becomes mobile, which leads to a breakage of the extended hydrogen bond network from the OEC mediated by W665. (vi) As a result of the above five structural changes, the ligands to the OEC (D61, D170, H332, and A344) slightly move and change their orientations. Among these changes, the displacement of W665 and insertion of O6 provides novel insights, particularly into the mechanism of the water splitting reaction (Fig. 5). In the S_1 state, W665 is located in the O4 channel (a 15 Å-long water channel beginning from the O4 of the OEC) and is hydrogen-bond with W567 (water molecule 567 which hydrogen-bonds with W665 and the O4). Upon a transition to the higher S_i-state, W665 becomes mobile which disrupts the hydrogen-bond with W567, with W567 moving towards the O4 by 0.2 Å to strengthen the hydrogen bond with the O4. This movement breaks the hydrogen bond network starting from O4 to the luminal surface of PSII, consistent with this hydrogen bond network works as a path for proton transfer [50], suggesting that the proton transfer has occurred through this network during the transition of the Kok-cycle ($S_1 \rightarrow S_2$ or $S_2 \rightarrow S_3$),

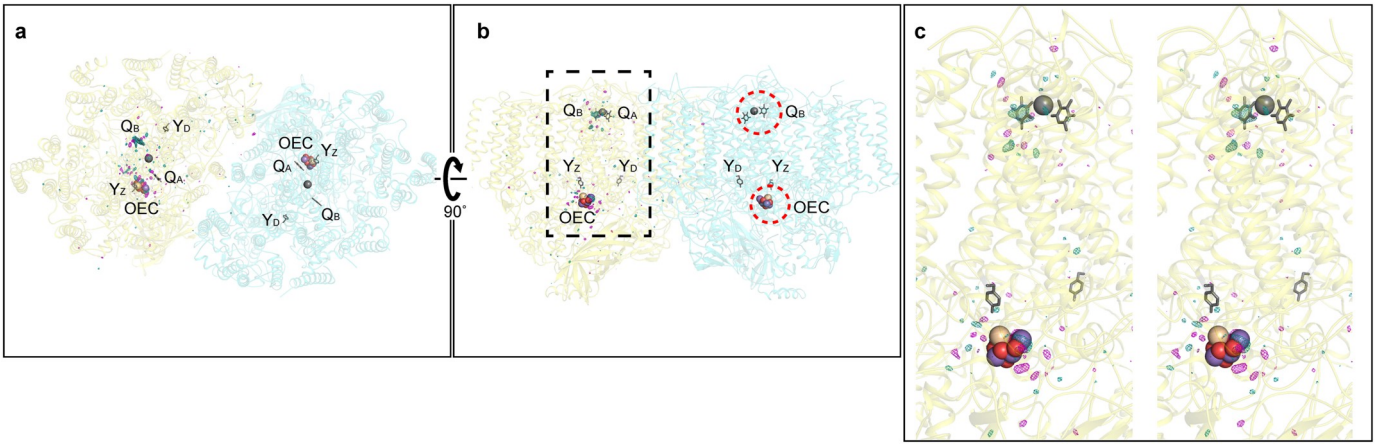

Fig. 3. Light-induced structural changes in PSII. The F_{obs} - F_{obs} isomorphous Fourier difference map between the S_3-state and the S_1 state contoured at ± 4.5 σ levels is shown in turquoise (positive) and magenta (negative) in the top **(a)** and side **(b)** views. Red dashed circles in (b) indicate two regions in which major difference peaks are localized. **(c)** Enlarged and stereo view of the region boxed by dashed lines in **(b)**. (For interpretation of the references to colour in this figure legend, the reader is referred to the web version of this article.)
This figure is modified from Suga et al. Nature, 543 (2017) 131.

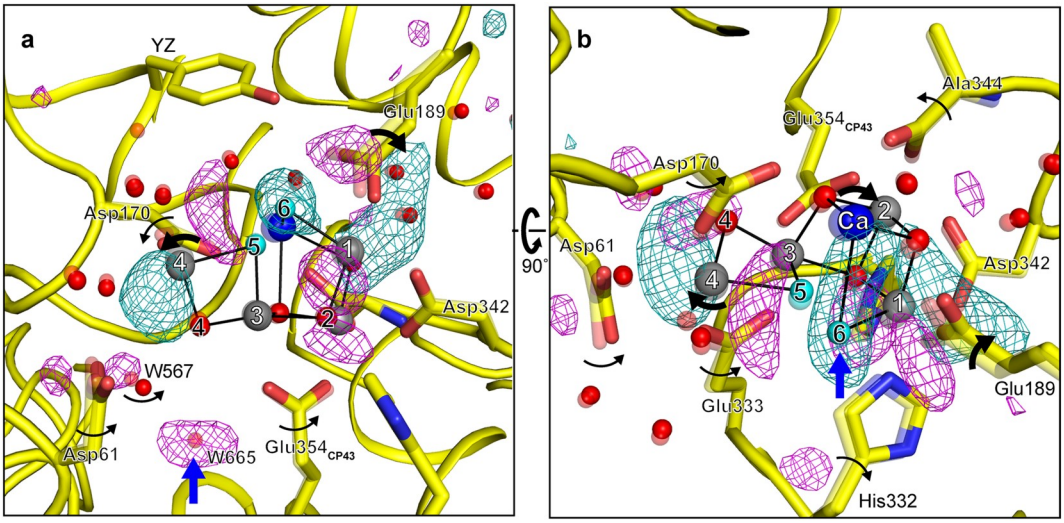

Fig. 4. Structural changes around the OEC during the transition from the S_1 to S_3 state. **(a, b)** The structures in the S_1 and the S_3 states are shown with the isomorphous difference Fourier map contoured at ± 5.0 σ levels in turquoise (positive) and magenta (negative) colors. The S_1 state structure where changes occurred during the progress of the Kok-cycle are shown in a transparent presentation and black arrows indicate corresponding structural changes. Blue arrows indicate the positions of O6 and W665. (For interpretation of the references to colour in this figure legend, the reader is referred to the web version of this article.)
This figure is modified from Suga et al. Nature, 543 (2017) 131.

and the breakage of the hydrogen bond network by displacement of W665 may provide a mechanism by which PSII avoids backflow of the released proton to the OEC. The insertion of O6 into the site between the O5 and Mn1 changes the OEC to a Mn_4CaO_6 cluster in the S_3 state. The distance between O6 and O5 is around 1.5–2.0 Å, which is suitable for the O═O bond formation. Theoretical calculation suggests possible chemical structure of the O6 and O5 atoms are (i) superoxide (1.3 Å), (ii) peroxo (1.5 Å), (iii) oxyl/oxo (2.0 Å), and (iv) hydrooxo/oxo (2.4 Å) [51], and the structure fits well with either peroxo and oxyl/oxo, but the assignment was not conclusive due to the limited resolution. In any case, the result therefore suggests that an O═O bond formation may occur between them. This reaction mechanism nicely explains why the OEC has the distorted chair structure with the unusually long bonded

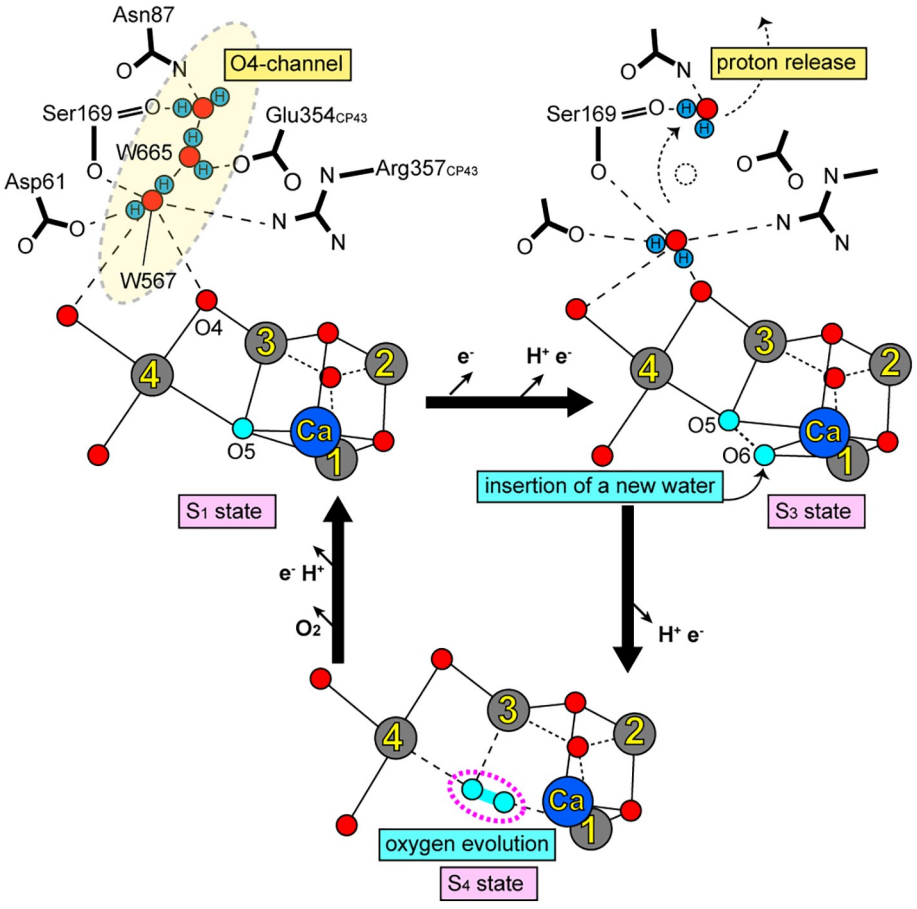

Fig. 5. A possible mechanism for the O═O bond formation and proton transfer pathways from the OEC. The dotted circle indicates increased mobility of the water molecule W665 next to the water W567 that is hydrogen-bonded with O4. The displacement of W665 results in the approach of W567 to O4 in the S_2 or S_3 state. The dot arrows indicate proton transfer in the O4-channel. A new water molecule O6 is inserted in the vicinity of O5 in the S_3 state. The oxygen atoms encircled by dashed pink lines represent the possible site of O═O bond formation. (For interpretation of the references to colour in this figure legend, the reader is referred to the web version of this article.)

form of O5 [22,31–33,52].

2.4. Structural insights into the mechanism of water splitting reaction revealed by XFEL irradiation

Since the birth of XFEL sources which provide femtosecond X-ray pulses with a billion-folds greater brilliance than SR X-rays, the new opportunity to study the damage free structure of PSII and its structural dynamics was brought to us. It is known that the OEC adjusted the structure finely during the Kok-cycle thereby enabling the water splitting reaction under the mild environmental conditions. The damage free structure in the S_1 state analyzed by SF-ROX shows the distorted chair form structure of the OEC with particularly long Mn−O distances for the O5 atom, and also the structure in the intermediate S_3 state analyzed by time-resolved SFX demonstrates the insertion of a new water molecule (O6) into the OEC for the O═O bond formation in a position nearby (O5). These results have provided substantial progress for our understanding of the water splitting reaction mechanism occurring in nature. It is our hope that these structural insights not only greatly advance our understanding on the photosynthetic water splitting reaction but may also provide important clues for rational designs of artificial catalysts that can be used to oxidize water by visible light through which, clean and renewable energy may be obtained.

3. Bovine cytochrome *c* oxidase

3.1. Introduction of cytochrome c oxidase

In cell respiration of almost all aerobic organisms including mammalian, cytochrome *c* oxidase (CcO), terminal oxidase in the respiratory chain is the most important protein complex, where protons from the mitochondrial matrix move to outside of the mitochondrial inner membrane, driven by reduction of O_2 to water [53,54]. Since the proton motive force generated by respiratory chain complexes is utilized for ATP synthesis, understanding the mechanism of linkage between proton-pumping and the redox reaction by CcO has been a significant subject in bioenergetics and bioinorganic chemistry fields. CcO from bovine heart includes 4 metal sites (Cu_A, heme *a*, heme a_3 and Cu_B) for O_2 reduction, with the O_2 reduction site comprising of Fe_{a3} of heme a_3 and Cu_B (Fig. 6a and b). The structure of the O_2 reduction site defines 6 distinguishable intermediates (R, A, P, F, O and E-form) in a reaction turnover (Fig. 6c) [53,54]. The X-ray crystallographic analysis of CcO from bovine heart muscle in resting and reduced state revealed the structure of these metal site and possible amino acid residues involving intramolecular electron transfer and redox-coupled proton pumping [55–57]. The protein sample of CcO for X-ray structural analysis was natively purified from bovine heart as a resting oxidized form which stops turnover due to a peroxide bridging between the Fe_{a3} and Cu_B and is not involved in the catalytic cycle. Although the resting oxidized form is absolutely stable without addition of any reductants, it is easy to fully reduce the O_2 reduction site by some reductants to produce R-form ($Fe_{a3}{}^{2+}$ and $Cu_B{}^{1+}$) which has no exogeneous ligand [58–60]. R-form of CcO binds molecular oxygen (O_2), yielding an oxygenated intermediate ($Fe_{a3}{}^{2+}$–O_2), A-form. O_2 is reduced by 4 electrons from Fe_{a3}, Cu_B and Y244 to be converted to water via the reaction intermediates of P, F, O and E (Fig. 6c) [53,61]. Y244 is the conserved residue and covalently linked to one of the histidines coordinated to Cu_B. Structures of these intermediates in O_2 reduction site were established by time-resolved resonance Raman spectroscopy [62–64]. The Fe−O stretching frequencies of Raman band were determined for all the intermediates. Stoichiometric analysis revealed that each proton is transferred out of the membrane (P-side), coupled with each electron transfer from cytochrome *c* via Cu_A and Fe_a to O_2 bound on Fe_{a3} (i.e. 4 protons are pumped per an enzymatic turnover) [65–68]. X-ray structural analyses of bovine CcO at various oxidation and ligand-binding states [69] and other spectroscopic analyses including optical absorption [61], electron paramagnetic resonance (EPR) [60] and infrared (IR) [70–73] have provided significant insights into the structures of catalytic intermediates and mechanism of proton pumping and O_2 reduction. However, the mechanism of highly efficient proton pumping coupled with electron transfer (H^+/e^- ratio of 1.0) and unidirectional proton pumping are still unclear, because the effects of structural change in O_2 reduction site on the dynamics of the proton transfer pathway is not fully understood.

In the well-studied CcO from bovine heart, protons used for the chemical reaction to reduce O_2 are transferred through proton conducting pathways known as the D- and K-pathway, towards the O_2 reduction site from the mitochondrial matrix (N-side) [53,54]. On the other hand, protons are transferred through another proton conducting pathway, H-pathway, composed of a water channel and a hydrogen-bond network (Fig. 6b) [54,69]. Since the water channel contains several water cavities, in which water molecules can migrate thermodynamically, protons are transferred as hydronium ions through the water cavities from the N-side to the formyl group of heme *a* which is located at the bottom end of the hydrogen bond network. Comparison of the high resolution crystal structures revealed that helix X, involved in the formation of the H-pathway, has two types of structures (Fig. 6d) [69,74]. The structure in the R-form shows the open structure of the H-pathway with a water cavity between helix X and heme *a*. In contrast, the resting oxidized or ligand-binding form shows that the backbone C═O of S382, in helix X, occupies the space for this water cavity to prevent water molecules from reaching the hydrogen-bond network (referred to as the closed conformation). Thus, it was suggested that the conformation of helix X regulates the open/closed structure of the H-pathway to suppress the proton back-leakage via the water channel [69,74].

Since the H-pathway is closed when any ligand binds to Fe_{a3}, protons have to be incorporated into CcO before O_2-binding in the R-form can occur in order to close the H-pathway. Moreover, protons should be temporarily stored in CcO until proton-pumping, coupled with sequential electron transfer from cytochrome *c* via Cu_A and heme *a* to O_2 bound on Fe_{a3}, occurs. A Mg-containing water cluster, which is isolated from the bulk solvent region and connected via hydrogen bonds to the hydrogen-bond network of the H-pathway, has been identified (Fig. 6b) [74]. This water cluster contains ca. 20 water molecules and various hydrophilic side chains, enough to store four temporary excess positive charges. From these findings, it is proposed that the water cavity is disappeared by O_2 binding to Fe_{a3}, after incorporation of 4 protons into the water cluster. The electrostatic repulsion between the stored protons and the positive charge of Fe_a, created upon donating an electron equivalent to reduce O_2 bound on Fe_{a3}, then drives proton-transfer from the water cluster to the hydrogen-bond network of the H-pathway. A proton transferred to the hydrogen-bond network is unidirectionally pumped to the P-side because the water channel is closed. Therefore, for highly efficient proton-pumping, timely closure of the H-pathway, by the conformational change of helix X from open to closed conformation, must be executed after the collection of 4 protons. In this section, we focus on the methods and results of structural analysis using XFEL to understand the mechanism of the H-pathway closure upon ligand binding to $Fe_{a3}{}^{2+}$ [24].

3.2. Time-resolved XFEL analysis for determining a short-life intermediate structure

For time-resolved analysis, it is necessary to synchronize rigorously the reactions of CcO molecules in a crystal. The preparation of CO-bound reduced CcO crystal was well established, and it was known that the CO bound to Fe_{a3} in reduced CcO is readily dissociated from the O_2 reduction site by visible laser irradiation [70,71,75]. Since the structural changes of CcO in a crystal, upon CO release, remain synchronized when laser irradiation is used to advance them, time-resolved analysis is possible. Capturing the structural snapshots of CcO by X-ray

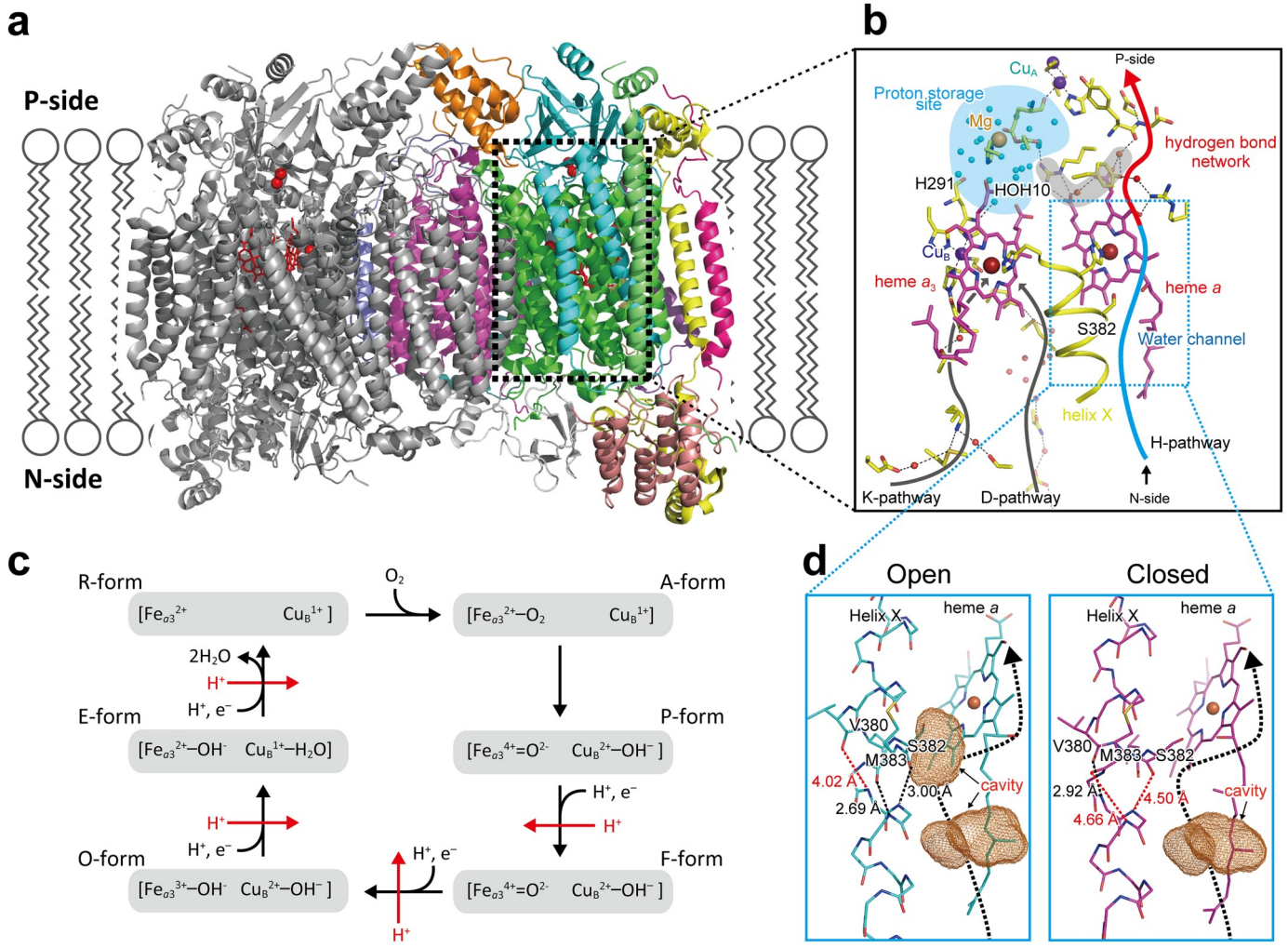

Fig. 6. The structure of the H-pathway in bovine heart CcO. (a) Overall structure of bovine heart CcO in dimeric state is shown. A monomer is colored and another one is shown in gray. (b) The locations of the water channel and the hydrogen-bond network composing the H-pathway are shown by the blue and red curves. The short hydrogen bond network (a gray area) connects the hydrogen bond network of the H-pathway and the proton storage site (the blue area). A water molecule in the proton storage site marked by HOH 10 forms a hydrogen bond to H291. (c) The reaction cycle of CcO represented by the redox state of O_2 reduction site. The protons for pumping are shown by red font and arrow, while the protons for chemical reaction are in black. (d) Water cavities are marked by brown cages. Helix X structures of the closed structure with two bulges at S382 and M383 and the open structure with one bulge at V380 are given in the right and left panels. These bulges are marked by red dotted lines. The broken arrows indicate the location of the water channel which includes the water cavities (brown cages). The channel extends up to R38 at the N-side end of the hydrogen bond network of the H-pathway and hydrogen bonded to the formyl group of heme *a*. (For interpretation of the references to colour in this figure legend, the reader is referred to the web version of this article.)
This figure was originally published in the Science Advances. Shimada A., et al. (2017) *Sci. Adv.*, **3**, e1603042, doi: https://doi.org/10.1126/sciadv.1603042.

crystallography in the CO-release process upon photodissociation is to see the reverse process of the structural changes coupled with the O_2 binding. For a high resolution X-ray dataset, crystal size should be as large as possible. For capturing the structural changes of protein moiety, the X-ray data collection under non-cryo condition is necessary. SF-ROX [23,42] can meet both these needs if it is combined with the humid air and glue coating (HAG) method, which prevents the loss of the diffraction spot quality and resolution caused by drying up of crystals [76].

Before the pump-probe time-resolved XFEL measurements, the visible laser (pump laser) energy for complete photodissociation of the CO from O_2 reduction site was determined by analyzing the visible absorption spectroscopy of the crystalline sample. Furthermore, the enzymatic reaction dynamics of CcO in the crystalline state is likely to differ from that in soluble state because the flexibilities of protein moieties are restricted by the molecular packing in crystalline. Thus, the decision of a desirable time-point, based on the time-course of spectral changes in crystalline state, is prerequisite to the XFEL data collections. Although the visible absorption spectroscopy is a useful tool for obtaining the kinetics of photodissociation of CO from Fe_{a3}, it does not provide the kinetics of transient CO-binding to Cu_B, after dissociation from Fe_{a3}. The time-resolved infrared (IR) spectroscopy is a unique technique for this purpose. In Fig. 7, the time-resolved IR spectral changes are traced from 20 ns to 500 ms after photodissociation of CO from the O_2 reduction site. They were measured using a recently developed highly sensitive IR spectrometer [73]. CO stretch band of CO-Cu_B (~2060 cm^{-1}) appeared at 20 ns after pump laser irradiation coincidentally with the disappearance of that of CO-Fe_{a3} (~1960 cm^{-1}), and the intensity of the CO stretch band of CO-Cu_B did not change within 100 ns (Fig. 7a and b). Biphasic CO-release was observed with 76% of CO molecules released from Cu_B at τ = 4.4 μs with 24% residual types of these released much slower (τ = 12.8 ms). The released CO was then shown to rebind to Fe_{a3} at τ = 6.2 ms and 34.0 ms; the dissociation kinetics in crystal are different from in solution reported before [70,71,73,77] (i.e., the time constant of CO release from Cu_B is determined to be 1.5–1.6 μs in solution, whereas that in crystal is 4.4 μs).

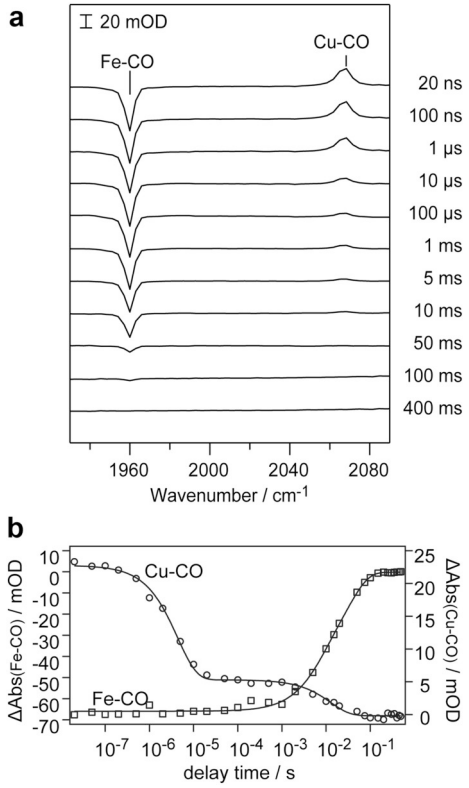

Fig. 7. CO ligand dynamics initiated upon CO photodissociation of CcO in the crystalline phase at 4 °C. (a) Time-resolved IR difference spectra upon CO photodissociation. Each difference spectrum was obtained by subtracting the probe-only (CO-bound) spectrum. (b) Temporal changes in the Fe-CO and Cu-CO intensities. (For interpretation of the references to colour in this figure legend, the reader is referred to the web version of this article.)
This figure was originally published in the Science Advances. Shimada A., et al. (2017) *Sci. Adv.*, **3**, e1603042, doi: https://doi.org/10.1126/sciadv.1603042.

Based on these spectral results, diffraction data was collected at 20 ns and 100 μs after flash photodissociation of CO to obtain the structural information of both CO bound to Cu_B and released from Cu_B.

Following to the protocol of the SF-ROX measurements, a CcO crystal was rotated by a small angle in a stepwise fashion to collect still diffraction images that are discrete and sequential in the course of the crystal rotation. Each XFEL irradiation spot is separated with 50 μm to avoid XFEL radiation damage. For measuring diffraction spots with sufficient data completeness, 40, 24 and 43 crystals were used in the condition before pump-laser irradiation (abbreviated as "dark" hereafter), at 20 ns and 100 μs after flash photodissociation of CO, respectively. Each crystal structure of "dark", 20 ns and 100 μs after flash photodissociation, was successfully determined at 2.2, 2.4 and 2.2 Å resolution, respectively.

3.3. CO migration in the O_2 reduction site

F_{obs}-F_{calc} difference Fourier map calculated without CO molecule in the O_2 reduction site revealed that CO bound to Fe_{a3} in "dark", whereas CO migrated to Cu_B at 20 ns and was released from the O_2 reduction site at 100 μs after photodissociation (Fig. 8a). Although any significant residual densities of CO were not detected at 100 μs at 3.5 σ level, the weak positive density was observed around Cu_B at 100 μs as mentioned below. $F_{obs(20ns)}$-$F_{obs(dark)}$ and $F_{obs(100μs)}$-$F_{obs(dark)}$ maps showed clearly the movement of CO from Fe_{a3} via Cu_B to the outside of the O_2 reduction site (Fig. 8b). Furthermore, the migration of Cu_B towards Fe_{a3} at 20 ns was detected as a pair of positive and negative densities around the Cu_B in Fig. 8b in $F_{obs(20ns)}$-$F_{obs(dark)}$ map. The geometry of the O_2 reduction site, at 20 ns after flash photodissociation, showed the shortest distance between Cu_B and Fe_{a3} and the largest migration of Cu_B from the trigonal plane among three datasets ("dark", 20 ns, and 100 μs), representing that the trigonal plane including Cu_B was perturbed at 20 ns (Fig. 8c). Since Cu_B in the trigonal plane consisted of nitrogen atoms of histidine coordinated to Cu_B, which is too stable to make an additional link with a ligand, it is suggested that the displacement of Cu_B from the plane is a prerequisite for the binding of CO at Cu_B.

In the structure refinement, the position of CO molecule at the O_2 reduction site was carefully evaluated from the resulting F_{obs}-F_{calc} difference Fourier map and comparison of atomic displacement parameters (B values) of CO with surrounding atoms (i.e. heme a_3, Fe_{a3} and Cu_B). The peak heights of CO in $F_{obs} - F_{cal}$ difference Fourier map of "dark", 20 ns, and 100 μs: 1.34, 0.99, and 0.22, respectively, were determined by calculating the ratio of the peak height of CO averaged that of two reference water molecules detected at full occupancy in any reported CcO structures (Table 1). The peak height of 0.22 near Cu_B at 100 μs after photodissociation is consistent with IR results which shows the presence of residual (24%) CO bound to Cu_B at 100 μs. When 100% occupancy of CO for "dark" and 20 ns, obtained from IR analysis, was used for the structure refinement with XFEL data, CO bound to Cu_B at 20 ns was characterized by higher temperature factors than CO bound to Fe_{a3} in "dark". Thus, information from the time-resolved analysis of both IR and XFEL are important to elucidate the property of CO moiety at each of the three states (Table 1).

3.4. The open/closed structure transition of H-pathway upon CO release

Although the location of heme a_3 was fixed because the propionate and hydroxyl-farnesylethyl groups interacted with surrounding hydrophilic side chains, the subtle but significant translational shift of the region of C-pyrrole ring of heme a_3 was observed upon CO-release from the O_2 reduction site (Fig. 9a). Superposition of the crystal structure of each state onto the fully reduced ligand-free structure, which adopts the open conformation of helix X, showed the same distance between the C_β atom of L381 in helix X and the vinyl group of heme a_3 as that at 100 μs (3.37 Å) (Fig. 9b). On the other hand, a shorter distance was observed in the structures of "dark" and 20 ns (3.06 and 3.13 Å, respectively). This repulsion by hydrophobic groups would mediate the transduction of the conformational change from $heme_{a3}$ to the region of V380 to G384 in helix X. Considering that the observed structural changes upon CO-photodissociation reflect the reverse process of O_2-binding, the binding of O_2 to Cu_B prior to the binding to Fe_{a3}, is proposed to trigger the translational shift of heme a_3 towards L381 in helix X, thereby leading to the transition of the closed conformation in the H-pathway.

Based on the F_{obs}-F_{calc} density maps at the helix X, the conformations of helix X in "dark" and 20 ns were revealed to be closed, indicating that S382 protrudes to eliminate the water cavity in the H-pathway (Fig. 10a and b). On the other hand, at 100 μs, the structure of helix X was mixed with 55% closed and 45% open conformation (Fig. 10c). If the CO-binding to Cu_B made the helix X in the closed conformation, the above-mentioned CO occupancy bound to Cu_B at 100 μs should be corresponding to the occupancy of closed conformation of helix X at 100 μs. However, the occupancy of CO (22.3%) bound to Cu_B differed from that of closed conformation of helix X (55%) at 100 μs (Table 1), representing that the conformational change was not perfectly concomitant with the CO-release from O_2 reduction site. Although the occupancy of CO bound to Cu_B was not in agreement with that of the closed conformation of helix X at 100 μs, it is plausible that CO-release from the O_2 reduction site drove the conformational change in helix X from closed conformation to open conformation.

From the time-resolved structural analysis using CO-bound CcO, the following relay system for the closing H-pathway is proposed. O_2 binding to Cu_B before Fe_{a3} drives the translational shift of heme a_3 close to helix X. The resulting van der Waals interaction between C_β atom of

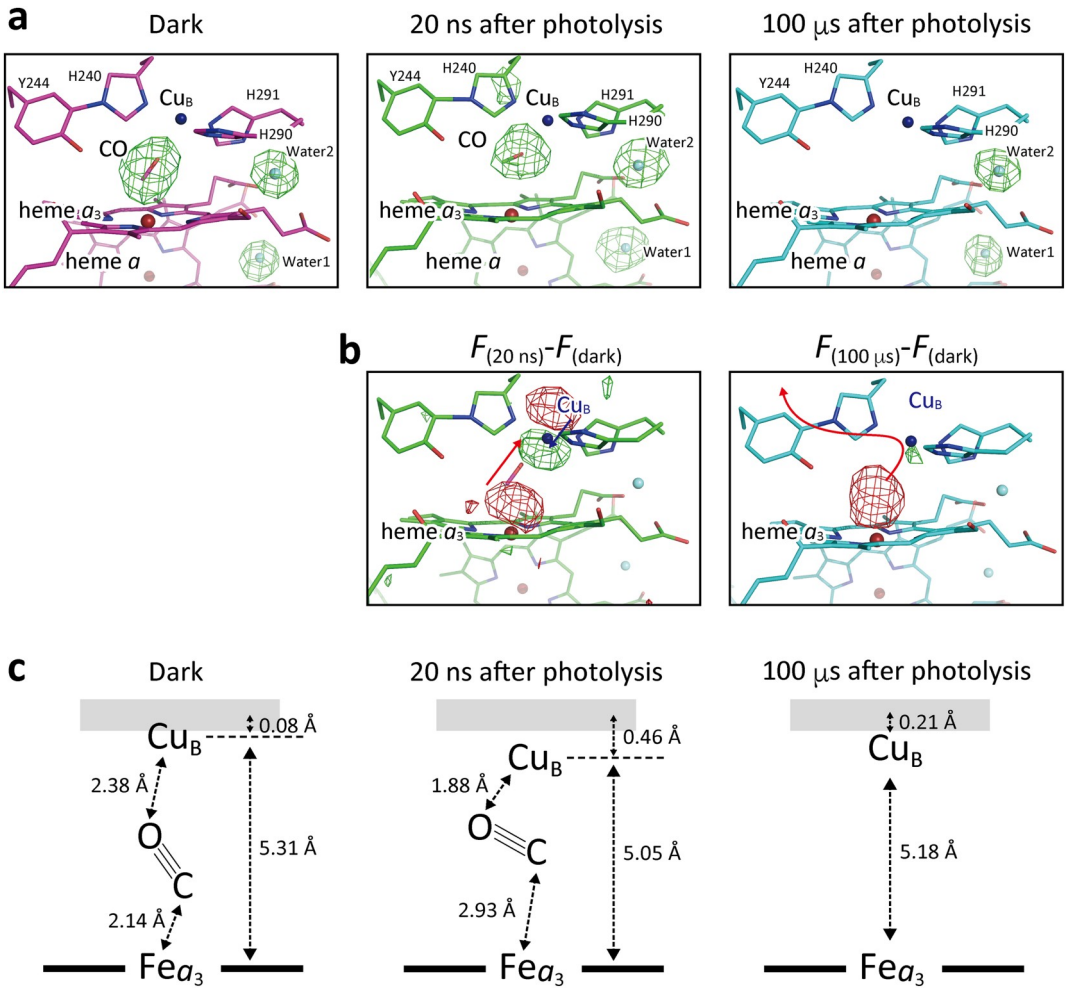

Fig. 8. Structures of the O_2 reduction site of the CO-bound fully reduced state at dark and at 20 ns and 100 μs after the photodissociation. (**a**) F_o-F_c difference electron density maps at 3.5 σ and structural models are illustrated. Purple, blue and light-blue spheres represent iron ions, copper ions and oxygen atoms of water molecules, respectively. Blue and red sticks indicate nitrogen and oxygen atoms, respectively. Red, green and light-blue sticks are the other atoms of the structures measured at dark and at 20 ns and 100 μs after photodissociation, respectively. CO, water 1 and water 2 were not included in the structure refinement. (Significant electron density assignable to the CO molecule between Fe_{a3} and Cu_B is not detectable in the 100 μs structure at the σ-level in the figure.) (**b**) The $F_{o(20\ ns\ or\ 100\ \mu s)}$ −$F_{o(dark)}$ difference electron density maps at +5.0/−5.0 σ level are shown as green/red mesh. The difference density maps show the directions of CO and Cu_B movements given by red and blue arrows, respectively. (**c**) Geometries of CO in the O_2 reduction site in the structures measured at dark and at 20 ns and 100 μs after photodissociation. Thick gray line at the top of each structure shows a side view of the Cu_B coordination plane consisting of three imidazole nitrogen atoms. (For interpretation of the references to colour in this figure legend, the reader is referred to the web version of this article.)
This figure was originally published in the Science Advances. Shimada A., et al. (2017) *Sci. Adv.*, **3**, e1603042, doi: https://doi.org/10.1126/sciadv.1603042.

Table 1
The peak height of CO molecule at O_2 reduction site.
This table was originally published in the Science Advances. Shimada A., et al. (2017) *Sci. Adv.*, **3**, e1603042, doi: https://doi.org/10.1126/sciadv.1603042.

	Dark	20 nsec	100 μsec
Reference water molecules			
Water1 (heme *a*) ($e^-/Å^3$)	0.472	0.269	0.395
Water2 (heme a_3) ($e^-/Å^3$)	0.472	0.373	0.406
Average ($e^-/Å^3$)	0.472	0.321	0.401
CO at Fe_{a3} ($e^-/Å^3$)	0.631		
CO at Cu_B ($e^-/Å^3$)		0.319	0.089
Ratio (CO/monitor)	1.337	0.994	0.222
Occupancy of CO (%)			
IR	100.0	100.0	24.0
X-ray	100.0	100.0	22.3

L381 belonging to helix X and the vinyl group of heme a_3 alters the conformation of helix X. As the conformational change of helix X from the open to the closed conformation occurs, the interaction between the O atom of S382 backbone and the N atom of V386 backbone is broken and then the backbone C═O group of S382 protrudes to the water cavity near the bottom end of the hydrogen bond network in the H-pathway.

3.5. *The structural basis assuring unidirectional proton transfer*

The process of structural changes upon CO-release determined by time-resolved XFEL analysis provides significant insights for understanding the unidirectional proton transfer mechanism as below. In R-form, where all metal sites are reduced and no ligands bind to the O_2 reduction site, protons are transferred from the N-side as hydronium ions through the water channel, then stored at the Mg-containing water cluster in the H-pathway (Fig. 11a). One of the water molecules (Wat101) in the water cluster links to H291 coordinated to Cu_B, suggesting that the proton saturation in the water cluster is sensed by Cu_B via H291 from the water molecule in the water cluster (Fig. 11b). H291 perturbs the trigonal plane including Cu_B, enhancing the sensitivity of Cu_B for coordinating with another ligand. O_2-binding to Cu_B initiates

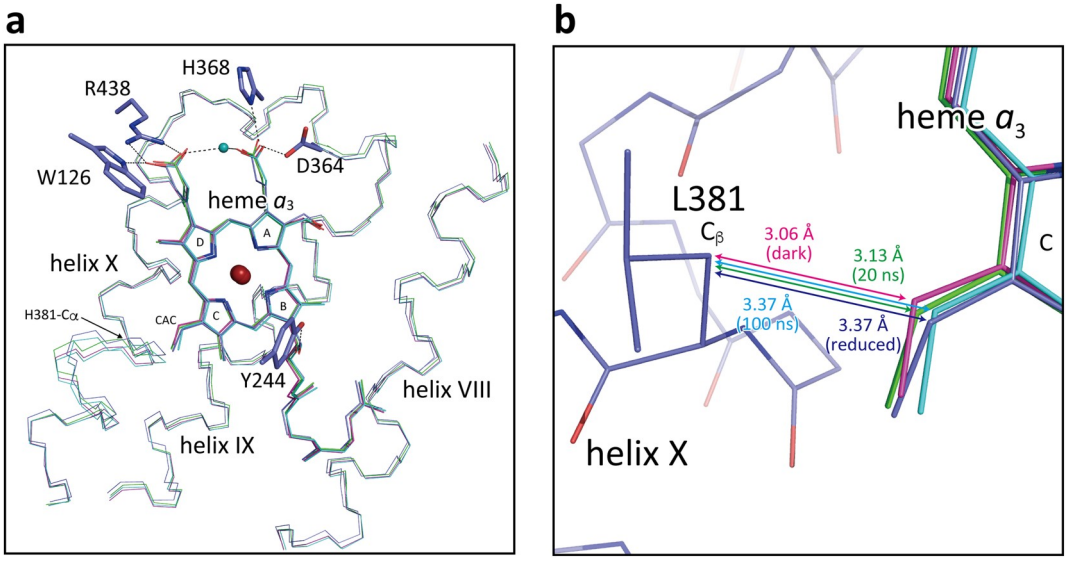

Fig. 9. Structural comparison of heme a_3 region in the structures measured at dark and at 20 ns and 100 μs after the photodissociation. (**a**) Each structure is superposed on that of the fully reduced ligand-free state (PDB ID, 5B1B) by least-squares fitting of the main chain atoms of subunit I. Red, green, light-blue and blue colors indicate the structures measured at dark, at 20 ns and 100 μs after photodissociation and at the ligand-free fully reduced state, respectively. Dark-blue sticks and red spheres of heme a_3 indicate nitrogen atoms and iron ions, respectively. The light blue sphere denotes the location of Water 2 shown in Fig. 8a. Amino acid side chains interacting with the heme a_3 by hydrogen bonds are drawn in thick stick models for the fully reduced state. These interactions are fully preserved in any time resolved structures. The characters, A, B, C and D, in the heme designate the PDB naming of the pyrrole rings. The CAC marks one of the carbon atoms of the vinyl group covalently bounded to the C-ring. (**b**) A close-up of the vinyl group regions in panel (a). The structures of heme a_3 and Cα drawings of protein regions at dark, 20 ns and 100 μs are illustrated using the same color code as in panel (a). Helix X of the ligand-free fully reduced state (PDB ID, 5B1B) is illustrated by a thin stick model, where oxygen atoms are red and the other atoms are blue. The distances between CAC and the β carbon of L381 at 20 ns (green) and 100 μs (blue) are given by the digits with arrows. (For interpretation of the references to colour in this figure legend, the reader is referred to the web version of this article.)
This figure was originally published in the Science Advances. Shimada A., et al. (2017) *Sci. Adv.*, **3**, e1603042, doi: https://doi.org/10.1126/sciadv.1603042.

the relay system as mentioned above; (i) translational shift of heme a_3 occurs, (ii) van der Waals interaction between L381 and vinyl group of heme a_3 alters the conformation of helix X, and (iii) protruded C=O of S382 towards the water cavity closes the H-pathway (Fig. 11c). After the closure of the water channel in the H-pathway, O_2 migrates to Fe_{a3} and is reduced by Fe_{a3}, followed by an electron transfer from Fe_a to the O_2 reduction site. The electrostatic repulsion between a proton stored in the water cluster and the positive charge created upon the oxidation of Fe_a drives unidirectional proton-pumping (Fig. 11d). This proton-pumping model is established only by the determination of the short-lived intermediate structure (CO binds to Cu_B) captured using XFEL time-resolved crystallography.

4. Nitric oxide reductase: cytochrome P450nor

4.1. Introduction

NO reduction is involved in denitrification by microorganisms growing in oxygen-limited environments [78]. The bacterial denitrifying system comprises of four reducing steps; $NO_3^- \rightarrow NO_2^- \rightarrow NO \rightarrow N_2O \rightarrow N_2$, with each step catalyzed by different enzymes [79,80]. The reducing equivalents for these reactions are provided from the respiratory chain coupling to the synthesis of adenosine triphosphate (ATP), and thus bacterial denitrification functions as anaerobic respiration. The mechanism of the NO reduction step that produces N_2O has received increasing attention because N_2O is the main stratospheric ozone-depleting substance [81–83]. N_2O is also a greenhouse gas. Even though the quantity of N_2O emissions released into the atmosphere is far less than that of carbon dioxide (CO) [81,84], its global warming potential is 300-times more potent than carbon dioxide over a 100-year time horizon [85,86]. In recent decades, as nitrogen fertilizer applications and nitrogen deposition have increased worldwide, global levels of N_2O have increased [87]. The changes in the nitrogen cycle and composition of the global atmosphere provides great implications for future global climate change.

In addition to bacteria, many fungi and yeasts also exhibit denitrifying activities [88,89]. P450nor is a heme enzyme isolated from the fungus *Fusarium oxysporum* [90]. The function of P450nor is the reduction of nitric oxide (NO) into nitrous oxide (N_2O) using NADH as an electron donor ($2NO + NADH + H^+ \rightarrow N_2O + NAD^+ + H_2O$) [91]. P450nor is a soluble enzyme (Fig. 12a) and its enzyme family is distinct from membrane-integrated bacterial NO reductases [92]. The reaction catalyzed by P450nor has two unique features among the P450 superfamily. Firstly, it is not a monoxygenase reaction using molecular oxygen. Secondly, P450nor active center can be reduced with hydride (H^-) directly from NADH [93]. In other members of P450, a small ferredoxin or a membrane-associated diflavin reductase supplies electrons to P450 [94].

The reaction scheme of P450nor has been proposed based on spectroscopic analysis [95–98]. As shown in Fig. 12b, the resting state of P450nor has a ferric heme with a water molecule and a Cys thiolate as axial ligands of iron [98]. In the first step, the water molecule at the sixth coordination site is displaced by NO, forming the ferric NO complex as an initial intermediate [97]. The ferric NO complex is then reduced with hydride (H^-) from NADH, producing the second intermediate, designated as intermediate-I (*I*) [95,97]. *I* is a two-electron reduced product of the ferric NO complex, although whether it is a singly or doubly protonated form is not clear. In the final step, *I* reacts with a second NO to generate the reaction product, N_2O [97]. Studies of model compounds, theoretical calculations [99–102] and X-ray crystallography [93,103] have supported this reaction mechanism. Early structural studies have reported the structure of P450nor in ferric NO complex at 1.8 Å resolution using data collected at synchrotron source from SPring-8 at 100 K [104]. However, X-ray induced radiation damage of protein crystals is well known to occur even at cryogenic temperatures [1,2], especially metal centers which are very rapidly reduced by the X-ray beam. The reduction of the heme iron greatly affects the geometry of the ligand molecule bound to metal ion.

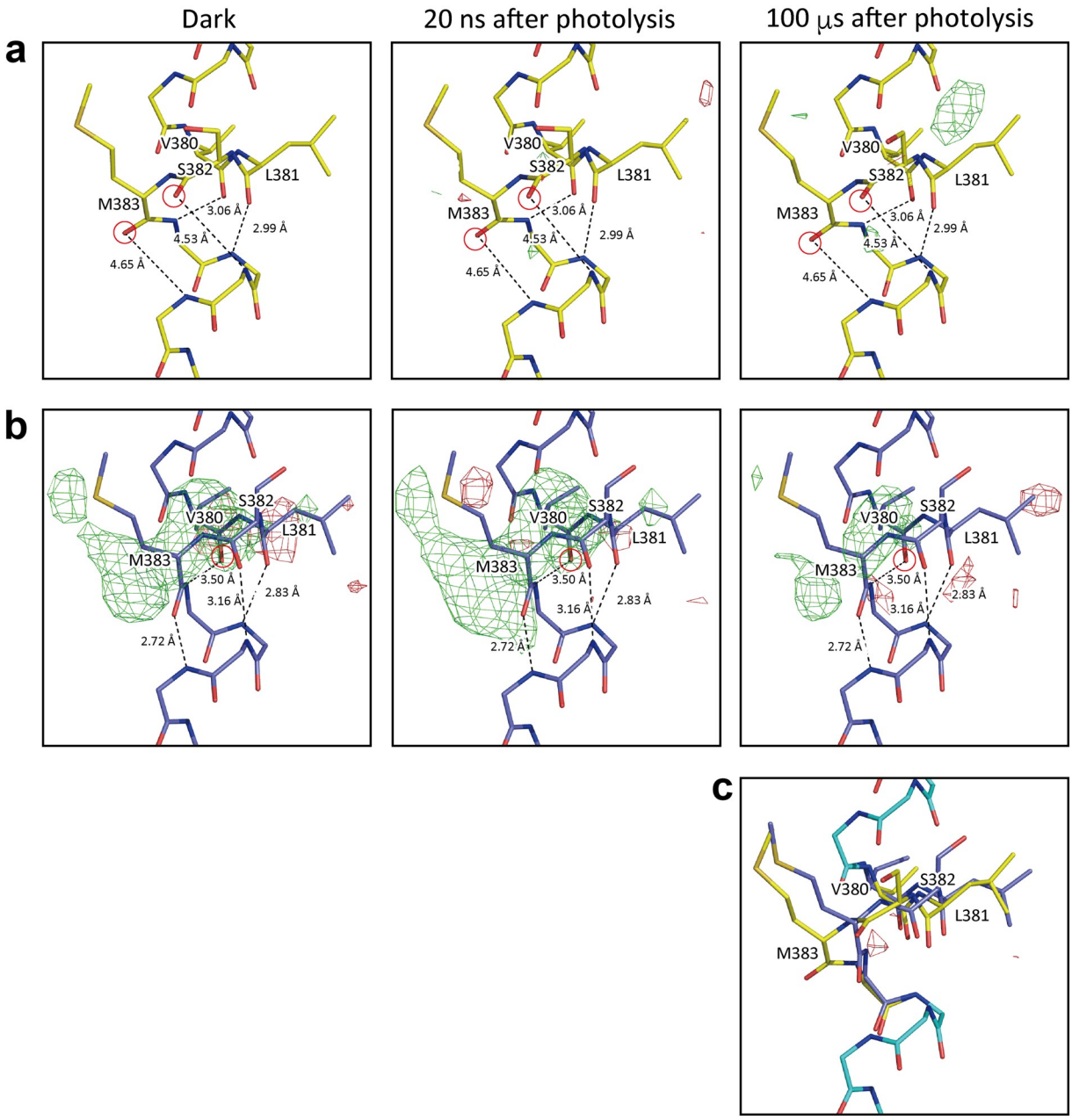

Fig. 10. F_{obs}-F_{calc} difference electron density maps of structures measured at dark and at 20 ns and 100 μs after the photodissociation. The structure factors of F_{calc} were calculated from the closed and open structures of helix X with two bulges at S382 and M383 (**a**) and with one bulge at V380 (**b**), and the F_{obs}-F_{calc} difference electron density maps were drawn at 3.5 σ together with the closed and open structures of helix X, respectively. The red circles mark the location of these bulges. (**c**) The F_{obs}-F_{calc} difference electron density map of the structure measured at 100 μs after photodissociation where structure factors of F_{calc} were calculated with multiple structures of helix X (55% closed structure with the two bulges and 45% open structure with the one bulge) and drawn at 3.5 σ together with the open and closed structures of helix X. (For interpretation of the references to colour in this figure legend, the reader is referred to the web version of this article.)
This figure was originally published in the Science Advances. Shimada A., et al. (2017) *Sci. Adv.*, **3**, e1603042, doi: https://doi.org/10.1126/sciadv.1603042.

Therefore, time-resolved analysis with SFX is an indispensable method for obtaining the precise and intact geometries of these intermediate states (initial ferric NO state and following intermediates). The new structural information combined with the data of time-resolved spectroscopy (UV–visible or IR spectroscopy) and theoretical calculations is necessary to fully understand the mechanism of enzymatic N_2O production by P450nor. More specifically, mechanism of NO-activation by hydride transfer from NADH, and the relationship between the electronic state of the protonated NO ligand and its reactivity for being attacked by the second NO molecule are interesting topics to be elucidated.

4.2. Use of caged NO for time-resolved experiments

The pump-probe technique with SFX using XFEL is a powerful tool for investigating protein structural dynamics if the target protein has a light-triggered reaction such as the case with PSII (See Section 2), photo-dissociation of ligand (i.e. CO) from the heme groups of hemoprotein (e.g. CcO or myoglobin [105]) (See Section 3), chromophore isomerization-driven reactions within photoactive yellow protein [106] or proton-pump bacteriorhodopsin [17,107,108]. If the enzyme is not light-sensitive, photosensitive caged compounds offer a crystallographic method to coherently initialize enzymatic reactions for time-resolved SFX. Their ability for time-resolved crystallography was first

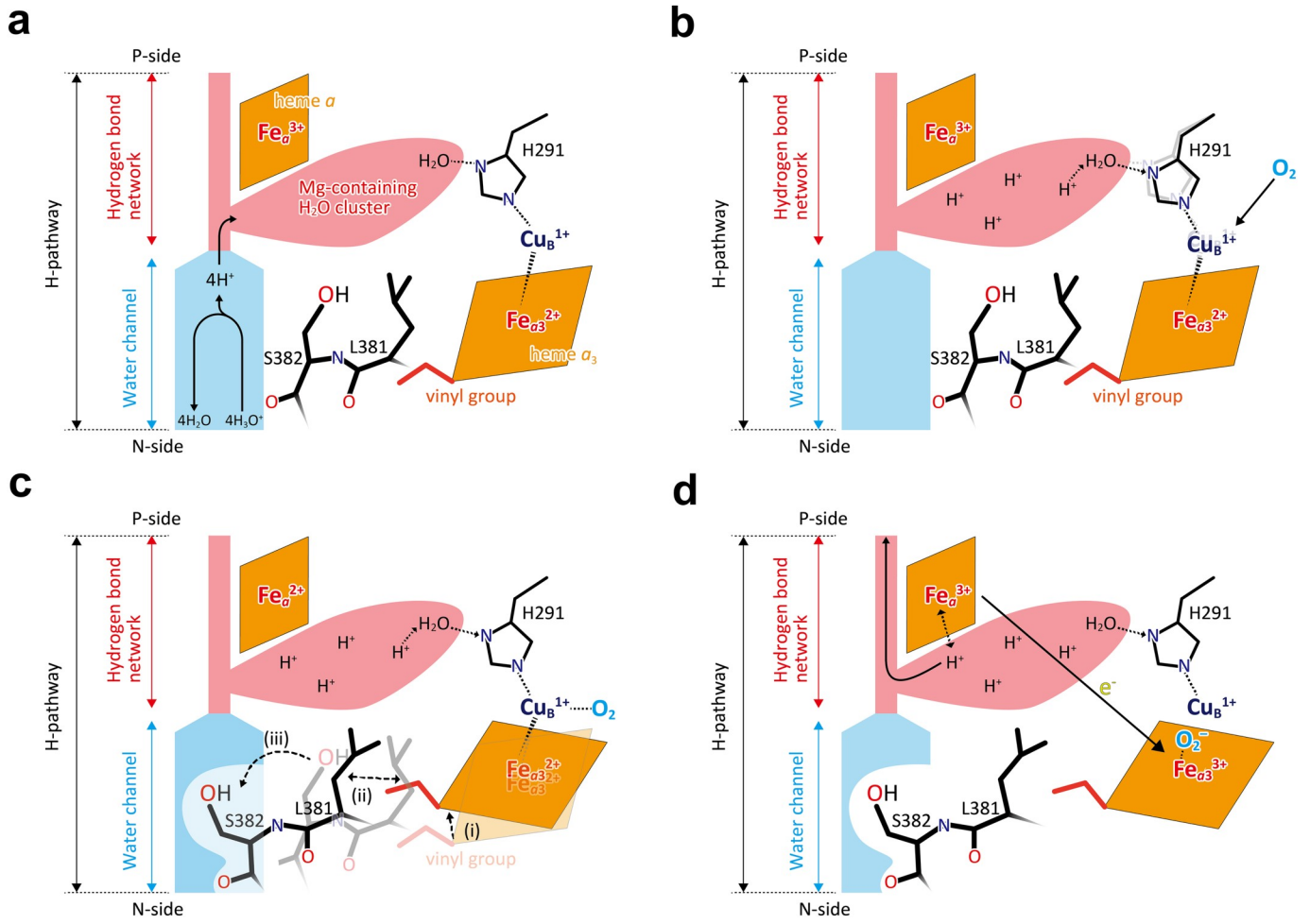

Fig. 11. A schematic representation of the water channel closure mechanism. (**a**) The water channel closure system in which the O_2 reduction site composed of Cu_B and Fe_{a3} is in the fully reduced state under turnover conditions. The Mg-containing H_2O cluster is the H^+-storage site which connects with Cu_B via H291 and a fixed water molecule (HOH10 in Fig. 6) in the storage site. The heme a_3 vinyl group is in van der Waals contact with L381. Protons are transferred by H_3O^+ through the open water channel. (**b**) Full protonation of the Mg-containing H_2O cluster promotes the protonation of the fixed water, resulting in the distortion of the regular trigonal coordination of Cu_B^{1+}. Then, this distortion increases the O_2-affinity of Cu_B^{1+}. (**c**) Closure of the water channel upon O_2 binding to Cu_B as follows; (i) migration of the plane of heme a_3; (ii) structural change of L381; and (iii) formation of the bulge at S382 to close the channel. (**d**) Proton pump after the channel closure. After migration of O_2 to Fe_{a3}, Fe_a^{2+} is oxidized to pump protons. (For interpretation of the references to colour in this figure legend, the reader is referred to the web version of this article.)
This figure was originally published in the Science Advances. Shimada A., et al. (2017) *Sci. Adv.*, **3**, e1603042, doi: https://doi.org/10.1126/sciadv.1603042.

demonstrated by an X-ray Laue diffraction [109]. Caged NO is useful as a reaction initiator for P450nor [110] since this compound can quantitatively release the NO on the microsecond time scale upon UV illumination (Fig. 13) and generate the ferric NO complex of P450nor at ambient temperature upon photolysis [25].

4.3. Enzyme kinetics in crystal

It is essential to characterize the reaction kinetics of P450nor in the crystalline phase prior to time-resolved SFX (as mentioned in the case of the CcO study). The visible and IR absorption spectroscopies at 293 K were performed to investigate the reaction kinetics in the crystalline phase. The time-resolved spectral changes in microcrystals of P450nor induced by UV pump illumination at 308 nm are shown in Fig. 14. The presence of a positive difference band at 437 nm indicates that the NO released from the caged-NO binds to heme at 20 ms (Fig. 14a). In the presence of NADH (Fig. 14b), after the NO-binding at 20 ms, another positive difference band was observed at 450 nm with the concomitant disappearance of the 437 nm band on the second time scale. The 450 nm band indicates the formation of *I* upon the reaction of the ferric NO complex with NADH [97]. Production of N_2O by NO reduction in the crystalline phase was demonstrated by the measurement of IR spectroscopy [25]. However, the reaction rate of *I* formation in crystal is approximately two orders of magnitude slower than in solution [97]. This difference was likely caused by the slow NADH-binding at the active site of P450nor due to crystal packing.

4.4. Capturing the initial intermediate using caged NO

For the SFX experiment of P450nor, hydroxyethyl cellulose [111] was included as a carrying medium into the solution containing both the microcrystals and caged-NO to generate a stable sample stream. Since this carrying medium is not fully transparent in the UV region and decreases the excitation efficiency of caged-NO by ~33%, the UV laser was irradiated from two directions at the same time for homogenous excitation. The XFEL pulse of SACLA irradiated the sample stream at 30 Hz, whereas the UV pump pulse illuminated it at 10 Hz. Thus, each diffraction image was obtained sequentially upon pump illumination ("light" data), followed by two diffraction images without the pump illumination ("dark1" and "dark2" data) with a time interval of 33.3 ms. NO is expected to be released only in the "light" data. Advantage of collecting "dark" datasets is a reduction of systematic errors

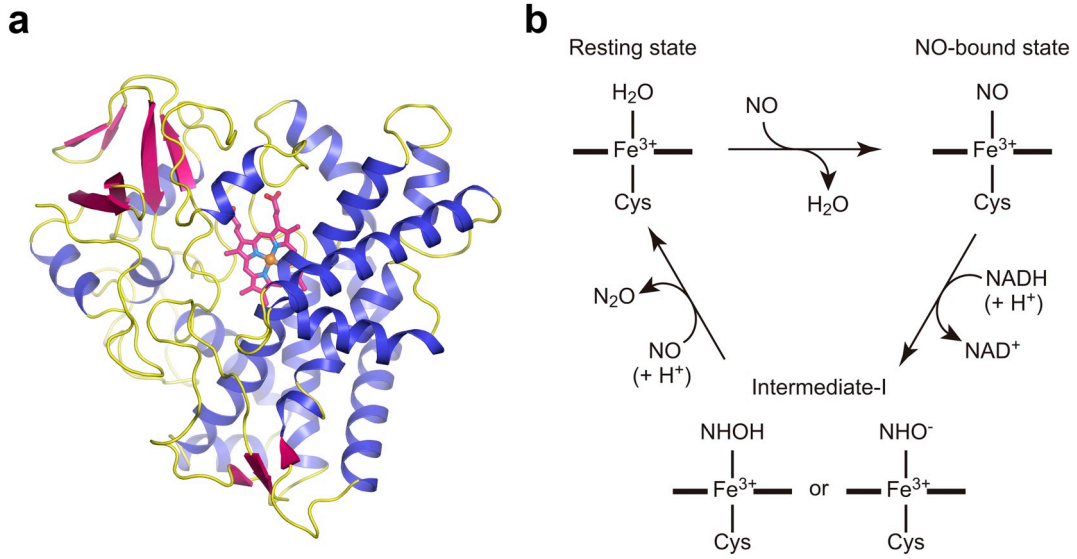

Fig. 12. Structure and reaction cycle of P450nor. (**a**) overall structure of P450nor. (**b**) P450nor reduces NO to N_2O through the NO-bound state and intermediate-*I*. This figure is modified from Tosha et al. Nat. Commun., 8 (2017) 1585.

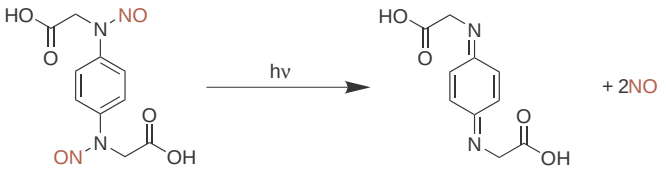

Fig. 13. Caged-NO photolysis. One caged-NO releases two NO molecules upon UV light illumination. (For interpretation of the references to colour in this figure legend, the reader is referred to the web version of this article.)
This figure is modified from Tosha et al. Nat. Commun., 8 (2017) 1585.

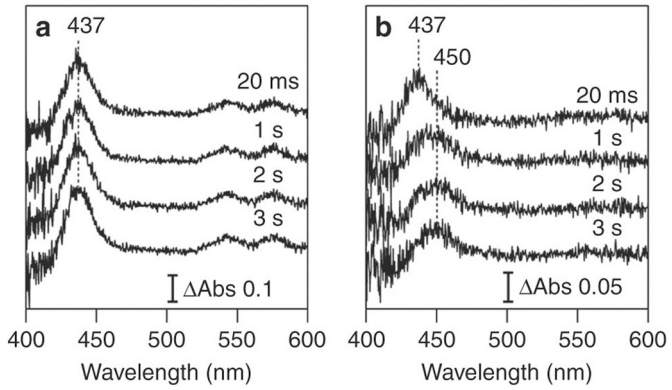

Fig. 14. Visible absorption spectra of microcrystal of P450nor. (**a**) Time-resolved visible absorption difference spectra of microcrystal after caged-NO photolysis in the absence of NADH and (**b**) in the presence of NADH. The difference was calculated by subtracting the spectrum recorded prior to photolysis. (For interpretation of the references to colour in this figure legend, the reader is referred to the web version of this article.)
This figure is modified from Tosha et al. Nat. Commun., 8 (2017) 1585.

derived from slight difference in the sample lot and conditions including the concentration of each composition (carrying media, NADH, microcrystals or caged NO). These errors would affect the quality of F_{obs} (light) – F_{obs} (dark) difference Fourier map. Two "dark" datasets should be collected to ensure that the scattering of pump laser for light data does not affect the other data.

Comparison of the active site of the resting enzyme and ferric NO complex as an initial intermediate (20 ms after photolysis) obtained by the SFX technique is illustrated in Fig. 15. In the structure of the resting state (Fig. 15a), a water molecule is bound to the ferric heme as a sixth ligand with 60% occupancy. The structure at 20 ms, after caged-NO photolysis, determined at 2.1 Å resolution is shown in Fig. 15b. The F_{obs} (light) – F_{obs} (dark2) difference Fourier map showed a strong positive electron density at the sixth heme coordination site (distal side), which was assigned to the bound NO. A small negative density between the Fe and S atom of C352 indicated that the iron atom was pulled towards the distal side of the heme by NO binding. The occupancy of the bound NO was estimated to 50%. Further increase of NO occupancy was not appropriate in this experiment because the UV pump energy had to be reduced to prevent laser damage to the crystal. The NO is bound to the iron in a slightly bent form (Fe-N-O angle of 158°) with a short Fe-NO distance (1.67 Å) compared to the damaged structures from data obtained by synchrotron radiation [25]. In addition, positive and negative difference densities were observed around A239, indicating a structural change with 0.2 Å movement by a steric repulsion between the bound NO and the main-chain carbonyl group (C = O) of A239 (Fig. 15c).

4.5. Next challenge: how to determine the next intermediate

In the reaction scheme in Fig. 12, ferric NO state is followed by the binding of NADH to form the next intermediate (*I*). As shown in Fig. 14, the formation of *I* from ferric NO state is a slow reaction in crystalline phase. The delay time of > 33 ms was out of range in the normal setting of time-resolved SFX measurement, because the illumination position of UV pump laser had to be very close to that of the XFEL pulse. Therefore, the measurement to obtain the next intermediate (*I*) requires another type of injector with a longer pathway between pump and probe positions. For example, Stagno et al. [112] used a mix-and-inject SFX system with a 10 s mixing delay to determine the intermediate state of the RNA riboswitch structure. The ligand solution and slurry of microcrystals in a HPLC line were fed into a T-junction mixer, which was connected to a gas-directed virtual nozzle through the long capillary to provide long delay times. Fuller et al. [113] used a tape drive device (conveyor belt system in combination with acoustic droplet ejection [114]) as a sample delivery and reaction initiation method to extend the range of delay time to 0.2–10 s in the time-resolved XFEL experiment. The conveyor belt continuously transports droplets containing crystal slurry through the reaction region, consisting of laser excitations for photochemical reactions or gas-activation. These two devices appear to be convertible to the measurement of intermediate (*I*) of

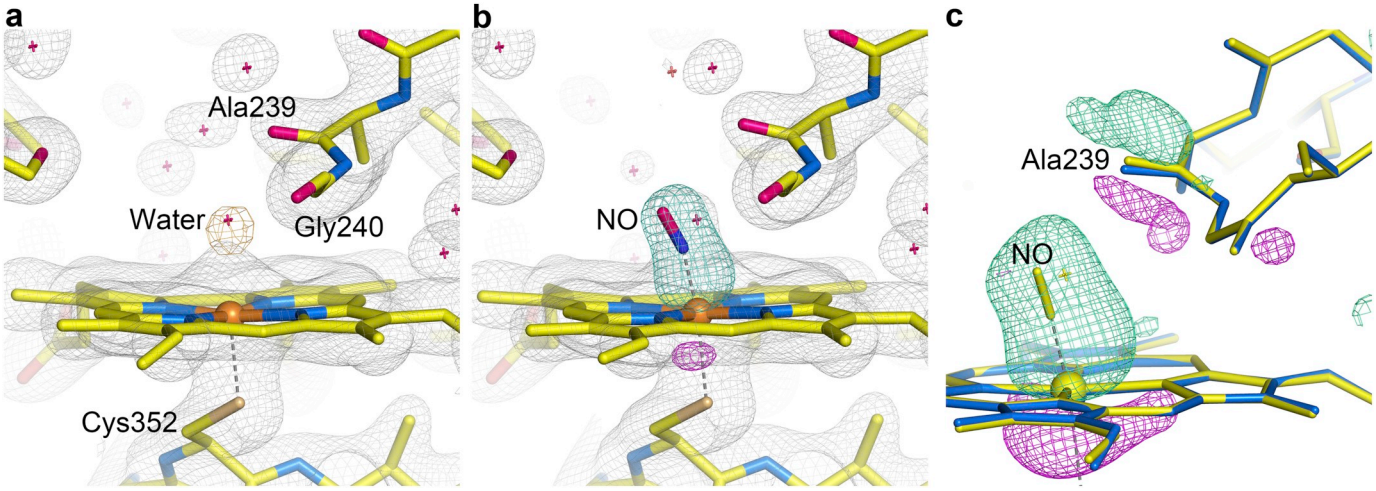

Fig. 15. SFX structures of P450nor. (**a**) Resting state structure using the "dark2" data. The $2F_{obs} - F_{calc}$ maps are shown in gray and contoured at 1.2 σ. The $F_{obs} - F_{calc}$ maps are shown in orange and contoured at 4.0 σ (**b**) Transient structures at 20 ms after caged-NO photolysis in the absence of NADH. (**c**) Superposition of the resting state (blue stick model) and at 20 ms after caged-NO photolysis (yellow stick model). The F_{obs}(light) − F_{obs}(dark2) difference Fourier maps are shown in turquoise (positive) and magenta (negative) and contoured at 6.5 σ in b and 2.8 σ in c. (For interpretation of the references to colour in this figure legend, the reader is referred to the web version of this article.)
This figure is modified from Tosha et al. Nat. Commun., 8 (2017) 1585.

P450nor. In addition to these injector-based techniques, a fixed-target sample delivery approach based on chip [115] or freeze-trapped methods would also be useful to take the snapshot of the reaction.

5. Future potential of time-resolved XFEL

Time-resolved analysis using XFEL offers a crystallographic method to visualize the process of enzymatic reactions. As shown in this review, successful application of SFX or SF-ROX for time-resolved analysis of photo-reaction or in conjunction with a photosensitive caged-compound were demonstrated. However, successful examples of time-resolved analyses measured at SACLA are currently limited to the proteins reviewed here in addition to bacteriorhodopsin [17,107]. Although the limited availability of beamtime is one of the reasons for the limited achievements, the start of the operation of second undulator beamline (BL2) at SACLA and the European XFEL from 2017 will accelerate further progress in time-resolved crystallography.

What is the technical bottleneck for its application to a wide range of samples? The key technical component that needs to be developed is the method of sample delivery. In the early stages of development, liquid-jet injectors were used for sample delivery in LCLS and SACLA [116,117]. Since then, a variety of delivery methods have been developed and used for SFX: viscous extruder (LCP-injector) [118–121], acoustic droplet ejection coupled with a conveyor belt drive [113], and fixed target systems [122] (The methods for sample delivery are reviewed by Grunbein et al. [123], and the technical challenges for membrane proteins with XFEL are reviewed by Standfuss [124] and Feld et al. [125]). These methods are designed to reduce the sample consumption and increase the hits of XFEL pulse with the crystal sample to obtain indexable diffraction images, which will provide us with more chance for obtaining the time-resolved datasets from limited amounts of sample.

Development of methods for a reaction trigger is also an important technical component for a wide-range of applications in time-resolved crystallography, since most of enzymatic reactions are not photosensitive (various methods are reviewed by Schlichting et al. [126]). Mixing of enzyme microcrystals with the substrate using a mixing injector, without using photo-trigger, has great potential [112,127], although the diffusion of substrate into the crystals takes a millisecond at least. As described in Section 4, use of caged compound can be a powerful tool for the initiation of the reaction. There are many caged compounds now commercially available (including ATP, other nucleotides, metals, amino acids and a variety of other substrates) [128,129]. However, not all of them may be suitable for time-resolved experiments. Most of them were originally developed for cellular or molecular biology experiments. The properties required for time-resolved experiments are a high efficiency yield of substrate releasing from the cage and a fast response rate upon the irradiation by pump laser (UV or visible light). On a practical level, the yield of uncaging is often decreased due to the attenuation of pump laser by the buffer composition or released substrate itself. The solubility and stability of caged compounds in carrying media at ambient temperature would also limit their concentration in the crystal. Design of an excellent caged substrate is thus necessary for application in a time-resolved experiment.

Finally, when conducting time-resolved experiments, attention must be directed to several experimental parameters. There will be many conflicts between both the solution and crystallization condition on the solubility and the substrate-binding affinity. The slow diffusion rate and restricted dynamics of a protein in the molecular packing in the crystal lattice results in a slower reaction rate, as shown in the P450nor (See Section 4.3). In addition, it is not easy to resolve multiple intermediates from electron density maps. In such a case, the quantitative information of the population of intermediates by spectroscopy is essential to determine the occupancy of each species. For the general application of studying conformational dynamics, the attachment of the photoreceptor into the protein and monitoring by UV–visible or fluorescence spectroscopy [130,131] is an important technique to analyze the fraction of each intermediate in both the solution and crystalline phase. Since the reaction conditions vary in each protein, a variety of crystal delivery and reaction initiation methods, as well as an equipped laboratory with a spectroscopic monitoring system, will broaden the possibility for future studies of time-resolved crystallography.

6. Conclusions

Three examples of time-resolved XFEL studies of metalloproteins were presented in this review. These studies provided a technical basis and future direction for time-resolved crystallography at XFEL. As shown in the PSII studies (Section 2) and the studies of bacteriorhodopsin [17,107,108], the pump-prove SFX method using microcrystals has been well-established for observation of the photo-driven

protein dynamics in photo-sensitive proteins. The CcO study described in Section 3 demonstrated that combinational use of the SF-ROX method and the HAG system is applicable to the pump-prove type time-resolved crystallography even for larger crystals. This technique is helpful to obtain a high-resolution data set. The photo-trigger methods used in CcO (Section 3) and P450nor (Section 4) showed that not only photo-sensitive protein like PSII but also non-photosensitive proteins can be analyzed by XFEL-based time-resolved crystallography. Since the CO ligand functions as a photolabile protecting group in many metalloproteins, including CcO, photoinduced dissociation of the CO ligand can be a trigger for time-resolved crystallography. Use of a photosensitive caged substrate has potential for a much wider application to time-resolved study. In order to succeed in observing the structural dynamics, it is crucial to determine the efficiency and kinetics of the protein reaction in the crystalline state by spectroscopic techniques as shown in the studies of CcO and P450nor. Currently several other sample delivery systems and reaction initiation methods are developed for time-resolved experiments in XFEL. Further improvement and development will open the possibility of time-resolved analyses for many important biological macromolecules.

Acknowledgements

The work described in this review was supported by JSPS (JP15H01642, JP17H05884 to M. S. and JP15H01655, JP17H05896 to H. S.)

References

[1] E.F. Garman, M. Weik, Radiation damage in macromolecular crystallography, Methods Mol. Biol. 1607 (2017) 467–489, https://doi.org/10.1007/978-1-4939-7000-1_20.
[2] J.M. Holton, A beginner's guide to radiation damage, J. Synchrotron Radiat. 16 (2009) 133–142, https://doi.org/10.1107/S0909049509004361.
[3] A. Gonzalez, C. Nave, Radiation damage in protein crystals at low temperature, Acta Crystallogr. D Biol. Crystallogr. 50 (1994) 874–877, https://doi.org/10.1107/S0907444994006311.
[4] M. Weik, R.B. Ravelli, G. Kryger, S. McSweeney, M.L. Raves, M. Harel, P. Gros, I. Silman, J. Kroon, J.L. Sussman, Specific chemical and structural damage to proteins produced by synchrotron radiation, Proc. Natl. Acad. Sci. U. S. A. 97 (2000) 623–628, https://doi.org/10.1073/pnas.97.2.623.
[5] T. Beitlich, K. Kuhnel, C. Schulze-Briese, R.L. Shoeman, I. Schlichting, Cryoradiolytic reduction of crystalline heme proteins: analysis by UV-vis spectroscopy and X-ray crystallography, J. Synchrotron Radiat. 14 (2007) 11–23, https://doi.org/10.1107/S0909049506049806.
[6] D. Kekilli, T. Moreno-Chicano, A.K. Chaplin, S. Horrell, F.S.N. Dworkowski, J.A.R. Worrall, R.W. Strange, M.A. Hough, Photoreduction and validation of haem-ligand intermediate states in protein crystals by in situ single-crystal spectroscopy and diffraction, IUCrJ 4 (2017) 263–270, https://doi.org/10.1107/S2052252517002159.
[7] C.M. Casadei, A. Gumiero, C.L. Metcalfe, E.J. Murphy, J. Basran, M.G. Concilio, S.C. Teixeira, T.E. Schrader, A.J. Fielding, A. Ostermann, M.P. Blakeley, E.L. Raven, P.C. Moody, enzymes. Heme, Neutron cryo-crystallography captures the protonation state of ferryl heme in a peroxidase, Science 345 (2014) 193–197, https://doi.org/10.1126/science.1254398.
[8] G. Chreifi, E.L. Baxter, T. Doukov, A.E. Cohen, S.E. McPhillips, J. Song, Y.T. Meharenna, S.M. Soltis, T.L. Poulos, Crystal structure of the pristine peroxidase ferryl center and its relevance to proton-coupled electron transfer, Proc. Natl. Acad. Sci. U. S. A. 113 (2016) 1226–1231, https://doi.org/10.1073/pnas.1521664113.
[9] A. Gumiero, C.L. Metcalfe, A.R. Pearson, E.L. Raven, P.C. Moody, Nature of the ferryl heme in compounds I and II, J. Biol. Chem. 286 (2011) 1260–1268, https://doi.org/10.1074/jbc.M110.183483.
[10] P.C.E. Moody, E.L. Raven, The nature and reactivity of Ferryl Heme in compounds I and II, Acc. Chem. Res. 51 (2018) 427–435, https://doi.org/10.1021/acs.accounts.7b00463.
[11] L. Lomb, T.R. Barends, S. Kassemeyer, A. Aquila, S.W. Epp, B. Erk, L. Foucar, R. Hartmann, B. Rudek, D. Rolles, A. Rudenko, R.L. Shoeman, J. Andreasson, S. Bajt, M. Barthelmess, A. Barty, M.J. Bogan, C. Bostedt, J.D. Bozek, C. Caleman, R. Coffee, N. Coppola, D.P. Deponte, R.B. Doak, T. Ekeberg, H. Fleckenstein, P. Fromme, M. Gebhardt, H. Graafsma, L. Gumprecht, C.Y. Hampton, A. Hartmann, G. Hauser, H. Hirsemann, P. Holl, J.M. Holton, M.S. Hunter, W. Kabsch, N. Kimmel, R.A. Kirian, M. Liang, F.R. Maia, A. Meinhart, S. Marchesini, A.V. Martin, K. Nass, C. Reich, J. Schulz, M.M. Seibert, R. Sierra, H. Soltau, J.C. Spence, J. Steinbrener, F. Stellato, S. Stern, N. Timneanu, X. Wang, G. Weidenspointner, U. Weierstall, T.A. White, C. Wunderer, H.N. Chapman, J. Ullrich, L. Struder, I. Schlichting, Radiation damage in protein serial femtosecond crystallography using an x-ray free-electron laser, Phys. Rev. B Condens Matter Mater. Phys. 84 (2011) 214111, https://doi.org/10.1103/PhysRevB.84.214111.
[12] E. Mizohata, T. Nakane, Y. Fukuda, E. Nango, S. Iwata, Serial femtosecond crystallography at the SACLA: breakthrough to dynamic structural biology, Biophys. Rev. 10 (2018) 209–218, https://doi.org/10.1007/s12551-017-0344-9.
[13] I. Schlichting, Serial femtosecond crystallography: the first five years, IUCrJ 2 (2015) 246–255, https://doi.org/10.1107/S205225251402702X.
[14] R. Neutze, R. Wouts, D. van der Spoel, E. Weckert, J. Hajdu, Potential for biomolecular imaging with femtosecond X-ray pulses, Nature 406 (2000) 752–757, https://doi.org/10.1038/35021099.
[15] H.N. Chapman, P. Fromme, A. Barty, T.A. White, R.A. Kirian, A. Aquila, M.S. Hunter, J. Schulz, D.P. DePonte, U. Weierstall, R.B. Doak, F.R. Maia, A.V. Martin, I. Schlichting, L. Lomb, N. Coppola, R.L. Shoeman, S.W. Epp, R. Hartmann, D. Rolles, A. Rudenko, L. Foucar, N. Kimmel, G. Weidenspointner, P. Holl, M. Liang, M. Barthelmess, C. Caleman, S. Boutet, M.J. Bogan, J. Krzywinski, C. Bostedt, S. Bajt, L. Gumprecht, B. Rudek, B. Erk, C. Schmidt, A. Homke, C. Reich, D. Pietschner, L. Struder, G. Hauser, H. Gorke, J. Ullrich, S. Herrmann, G. Schaller, F. Schopper, H. Soltau, K.U. Kuhnel, M. Messerschmidt, J.D. Bozek, S.P. Hau-Riege, M. Frank, C.Y. Hampton, R.G. Sierra, D. Starodub, G.J. Williams, J. Hajdu, N. Timneanu, M.M. Seibert, J. Andreasson, A. Rocker, O. Jonsson, M. Svenda, S. Stern, K. Nass, R. Andritschke, C.D. Schroter, F. Krasniqi, M. Bott, K.E. Schmidt, X. Wang, I. Grotjohann, J.M. Holton, T.R. Barends, R. Neutze, S. Marchesini, R. Fromme, S. Schorb, D. Rupp, M. Adolph, T. Gorkhover, I. Andersson, H. Hirsemann, G. Potdevin, H. Graafsma, B. Nilsson, J.C. Spence, Femtosecond X-ray protein nanocrystallography, Nature 470 (2011) 73–77, https://doi.org/10.1038/nature09750.
[16] I. Martiel, H.M. Muller-Werkmeister, A.E. Cohen, Strategies for sample delivery for femtosecond crystallography, Acta Crystallogr. D Biol. Crystallogr. 75 (2019) 160–177, https://doi.org/10.1107/S2059798318017953.
[17] E. Nango, A. Royant, M. Kubo, T. Nakane, C. Wickstrand, T. Kimura, T. Tanaka, K. Tono, C. Song, R. Tanaka, T. Arima, A. Yamashita, J. Kobayashi, T. Hosaka, E. Mizohata, P. Nogly, M. Sugahara, D. Nam, T. Nomura, T. Shimamura, D. Im, T. Fujiwara, Y. Yamanaka, B. Jeon, T. Nishizawa, K. Oda, M. Fukuda, R. Andersson, P. Bath, R. Dods, J. Davidsson, S. Matsuoka, S. Kawatake, M. Murata, O. Nureki, S. Owada, T. Kameshima, T. Hatsui, Y. Joti, G. Schertler, M. Yabashi, A.N. Bondar, J. Standfuss, R. Neutze, S. Iwata, A three-dimensional movie of structural changes in bacteriorhodopsin, Science 354 (2016) 1552–1557, https://doi.org/10.1126/science.aah3497.
[18] J.C.H. Spence, XFELs for structure and dynamics in biology, IUCrJ 4 (2017) 322–339, https://doi.org/10.1107/S2052252517005760.
[19] W.B. O'Dell, A.M. Bodenheimer, F. Meilleur, Neutron protein crystallography: a complementary tool for locating hydrogens in proteins, Arch. Biochem. Biophys. 602 (2016) 48–60, https://doi.org/10.1016/j.abb.2015.11.033.
[20] F. Meilleur, L. Coates, J.M. Cuneo, A. Kovalevsky, A.A.D. Myles, The neutron macromolecular crystallography instruments at Oak Ridge National Laboratory: advances, challenges, and opportunities, Crystals 8 (2018), https://doi.org/10.3390/cryst8100388.
[21] T. Ishikawa, H. Aoyagi, T. Asaka, Y. Asano, N. Azumi, T. Bizen, H. Ego, K. Fukami, T. Fukui, Y. Furukawa, S. Goto, H. Hanaki, T. Hara, T. Hasegawa, T. Hatsui, A. Higashiya, T. Hirono, N. Hosoda, M. Ishii, T. Inagaki, Y. Inubushi, T. Itoga, Y. Joti, M. Kago, T. Kameshima, H. Kimura, Y. Kirihara, A. Kiyomichi, T. Kobayashi, C. Kondo, T. Kudo, H. Maesaka, X.M. Marechal, T. Masuda, S. Matsubara, T. Matsumoto, T. Matsushita, S. Matsui, M. Nagasono, N. Nariyama, H. Ohashi, T. Ohata, T. Ohshima, S. Ono, Y. Otake, C. Saji, T. Sakurai, T. Sato, K. Sawada, T. Seike, K. Shirasawa, T. Sugimoto, S. Suzuki, S. Takahashi, H. Takebe, K. Takeshita, K. Tamasaku, H. Tanaka, R. Tanaka, T. Tanaka, T. Togashi, K. Togawa, A. Tokuhisa, H. Tomizawa, K. Tono, K. Wu, M. Yabashi, M. Yamaga, A. Yamashita, K. Yanagida, C. Zhang, T. Shintake, H. Kitamura, N. Kumagai, A compact X-ray free-electron laser emitting in the sub-angstrom region, Nat. Photonics 6 (2012) 540–544, https://doi.org/10.1038/nphoton.2012.141.
[22] M. Suga, F. Akita, K. Hirata, G. Ueno, H. Murakami, Y. Nakajima, T. Shimizu, K. Yamashita, M. Yamamoto, H. Ago, J.-R. Shen, Native structure of photosystem II at 1.95 Å resolution viewed by femtosecond X-ray pulses, Nature 517 (2015) 99–103, https://doi.org/10.1038/nature13991.
[23] M. Suga, F. Akita, M. Sugahara, M. Kubo, Y. Nakajima, T. Nakane, K. Yamashita, Y. Umena, M. Nakabayashi, T. Yamane, T. Nakano, M. Suzuki, T. Masuda, S. Inoue, T. Kimura, T. Nomura, S. Yonekura, L.J. Yu, T. Sakamoto, T. Motomura, J.H. Chen, Y. Kato, T. Noguchi, K. Tono, Y. Joti, T. Kameshima, T. Hatsui, E. Nango, R. Tanaka, H. Naitow, Y. Matsuura, A. Yamashita, M. Yamamoto, O. Nureki, M. Yabashi, T. Ishikawa, S. Iwata, J.R. Shen, Light-induced structural changes and the site of O=O bond formation in PSII caught by XFEL, Nature, 543 (2017) 131–135, doi:https://doi.org/10.1038/nature21400.
[24] A. Shimada, M. Kubo, S. Baba, K. Yamashita, K. Hirata, G. Ueno, T. Nomura, T. Kimura, K. Shinzawa-Itoh, J. Baba, K. Hatano, Y. Eto, A. Miyamoto, H. Murakami, T. Kumasaka, S. Owada, K. Tono, M. Yabashi, Y. Yamaguchi, S. Yanagisawa, M. Sakaguchi, T. Ogura, R. Komiya, J. Yan, E. Yamashita, M. Yamamoto, H. Ago, S. Yoshikawa, T. Tsukihara, A nanosecond time-resolved XFEL analysis of structural changes associated with CO release from cytochrome C oxidase, Sci. Adv. 3 (2017), https://doi.org/10.1126/sciadv.1603042.
[25] T. Tosha, T. Nomura, T. Nishida, N. Saeki, K. Okubayashi, R. Yamagiwa, M. Sugahara, T. Nakane, K. Yamashita, K. Hirata, G. Ueno, T. Kimura, T. Hisano, K. Muramoto, H. Sawai, H. Takeda, E. Mizohata, A. Yamashita, Y. Kanematsu, Y. Takano, E. Nango, R. Tanaka, O. Nureki, O. Shoji, Y. Ikemoto, H. Murakami, S. Owada, K. Tono, M. Yabashi, M. Yamamoto, H. Ago, S. Iwata, H. Sugimoto,

Y. Shiro, M. Kubo, Capturing an initial intermediate during the P450nor enzymatic reaction using time-resolved XFEL crystallography and caged-substrate, Nat. Commun. 8 (2017) 1585, https://doi.org/10.1038/s41467-017-01702-1.
[26] B. Kok, B. Forbush, M. McGloin, Cooperation of charges in photosynthetic O_2 evolution-I. A linear four step mechanism, Photochem. Photobiol. 11 (1970) 457–475 https://www.ncbi.nlm.nih.gov/pubmed/5456273.
[27] N. Cox, D.A. Pantazis, F. Neese, W. Lubitz, Biological water oxidation, Acc. Chem. Res. 46 (2013) 1588–1596, https://doi.org/10.1021/ar3003249.
[28] H. Dau, M. Haumann, The manganese complex of photosystem II in its reaction cycle—basic framework and possible realization at the atomic level, Coord. Chem. Rev. 252 (2008) 273–295, https://doi.org/10.1016/j.ccr.2007.09.001.
[29] V.K. Yachandra, K. Sauer, M.P. Klein, Manganese cluster in photosynthesis: where plants oxidize water to dioxygen, Chem. Rev. 96 (1996) 2927–2950 https://www.ncbi.nlm.nih.gov/pubmed/11848846.
[30] J. Yano, V. Yachandra, Mn4Ca cluster in photosynthesis: where and how water is oxidized to dioxygen, Chem. Rev. 114 (2014) 4175–4205, https://doi.org/10.1021/cr4004874.
[31] Y. Umena, K. Kawakami, J.R. Shen, N. Kamiya, Crystal structure of oxygen-evolving photosystem II at a resolution of 1.9 Å, Nature 473 (2011) 55–60, https://doi.org/10.1038/nature09913.
[32] M.M. Najafpour, G. Renger, M. Holynska, A.N. Moghaddam, E.M. Aro, R. Carpentier, H. Nishihara, J.J. Eaton-Rye, J.R. Shen, S.I. Allakhverdiev, Manganese compounds as water-oxidizing catalysts: from the natural water-oxidizing complex to nanosized manganese oxide structures, Chem. Rev. 116 (2016) 2886–2936, https://doi.org/10.1021/acs.chemrev.5b00340.
[33] J.R. Shen, The structure of photosystem II and the mechanism of water oxidation in photosynthesis, Annu. Rev. Plant Biol. 66 (2015) 23–48, https://doi.org/10.1146/annurev-arplant-050312-120129.
[34] J. Yano, J. Kern, Y. Pushkar, K. Sauer, P. Glatzel, U. Bergmann, J. Messinger, A. Zouni, V.K. Yachandra, High-resolution structure of the photosynthetic Mn_4Ca catalyst from X-ray spectroscopy, Philos. Trans. R. Soc. Lond. Ser. B Biol. Sci. 363 (2008) 1139–1147, https://doi.org/10.1098/rstb.2007.2209.
[35] J. Yano, Y. Pushkar, P. Glatzel, A. Lewis, K. Sauer, J. Messinger, U. Bergmann, V. Yachandra, High-resolution Mn EXAFS of the oxygen-evolving complex in photosystem II: structural implications for the Mn_4Ca cluster, J. Am. Chem. Soc. 127 (2005) 14974–14975, https://doi.org/10.1021/ja054873a.
[36] W. Ames, D.A. Pantazis, V. Krewald, N. Cox, J. Messinger, W. Lubitz, F. Neese, Theoretical evaluation of structural models of the S_2 state in the oxygen evolving complex of photosystem II: protonation states and magnetic interactions, J. Am. Chem. Soc. 133 (2011) 19743–19757, https://doi.org/10.1021/ja2041805.
[37] H. Isobe, M. Shoji, S. Yamanaka, Y. Umena, K. Kawakami, N. Kamiya, J.R. Shen, K. Yamaguchi, Theoretical illumination of water-inserted structures of the $CaMn_4O_5$ cluster in the S_2 and S_3 states of oxygen-evolving complex of photosystem II: full geometry optimizations by B3LYP hybrid density functional, Dalton Trans. 41 (2012) 13727–13740, https://doi.org/10.1039/c2dt31420g.
[38] S. Luber, I. Rivalta, Y. Umena, K. Kawakami, J.R. Shen, N. Kamiya, G.W. Brudvig, V.S. Batista, S1-state model of the O2-evolving complex of photosystem II, Biochemistry 50 (2011) 6308–6311, https://doi.org/10.1021/bi200681q.
[39] J. Yano, J. Kern, K.D. Irrgang, M.J. Latimer, U. Bergmann, P. Glatzel, Y. Pushkar, J. Biesiadka, B. Loll, K. Sauer, J. Messinger, A. Zouni, V.K. Yachandra, X-ray damage to the Mn_4Ca complex in single crystals of photosystem II: a case study for metalloprotein crystallography, Proc. Natl. Acad. Sci. U. S. A. 102 (2005) 12047–12052, https://doi.org/10.1073/pnas.0505207102.
[40] D.W. Cruickshank, Remarks about protein structure precision, Acta Crystallogr. D Biol. Crystallogr. 55 (1999) 583–601, https://doi.org/10.1107/s0907444998012645.
[41] Y. Pushkar, J. Yano, K. Sauer, A. Boussac, V.K. Yachandra, Structural changes in the Mn_4Ca cluster and the mechanism of photosynthetic water splitting, Proc. Natl. Acad. Sci. U. S. A. 105 (2008) 1879–1884, https://doi.org/10.1073/pnas.0707092105.
[42] K. Hirata, K. Shinzawa-Itoh, N. Yano, S. Takemura, K. Kato, M. Hatanaka, K. Muramoto, T. Kawahara, T. Tsukihara, E. Yamashita, K. Tono, G. Ueno, T. Hikima, H. Murakami, Y. Inubushi, M. Yabashi, T. Ishikawa, M. Yamamoto, T. Ogura, H. Sugimoto, J.R. Shen, S. Yoshikawa, H. Ago, Determination of damage-free crystal structure of an X-ray-sensitive protein using an XFEL, Nat. Methods 11 (2014) 734–736, https://doi.org/10.1038/nmeth.2962.
[43] L.V. Kulik, B. Epel, W. Lubitz, J. Messinger, Electronic structure of the Mn_4O_xCa cluster in the S_0 and S_2 states of the oxygen-evolving complex of photosystem II based on pulse ^{55}Mn-ENDOR and EPR spectroscopy, J. Am. Chem. Soc. 129 (2007) 13421–13435, https://doi.org/10.1021/ja071487f.
[44] J.P. McEvoy, G.W. Brudvig, Water-splitting chemistry of photosystem II, Chem. Rev. 106 (2006) 4455–4483, https://doi.org/10.1021/cr0204294.
[45] J. Messinger, M. Badger, T. Wydrzynski, Detection of one slowly exchanging substrate water molecule in the S_3 state of photosystem II, Proc. Natl. Acad. Sci. U. S. A. 92 (1995) 3209–3213, https://doi.org/10.1073/pnas.92.8.3209.
[46] J. Kern, R. Tran, R. Alonso-Mori, S. Koroidov, N. Echols, J. Hattne, M. Ibrahim, S. Gul, H. Laksmono, R.G. Sierra, R.J. Gildea, G. Han, J. Hellmich, B. Lassalle-Kaiser, R. Chatterjee, A.S. Brewster, C.A. Stan, C. Glockner, A. Lampe, D. DiFiore, D. Milathianaki, A.R. Fry, M.M. Seibert, J.E. Koglin, E. Gallo, J. Uhlig, D. Sokaras, T.C. Weng, P.H. Zwart, D.E. Skinner, M.J. Bogan, M. Messerschmidt, P. Glatzel, G.J. Williams, S. Boutet, P.D. Adams, A. Zouni, J. Messinger, N.K. Sauter, U. Bergmann, J. Yano, V.K. Yachandra, Taking snapshots of photosynthetic water oxidation using femtosecond X-ray diffraction and spectroscopy, Nat. Commun. 5 (2014) 4371, https://doi.org/10.1038/ncomms5371.
[47] C. Kupitz, S. Basu, I. Grotjohann, R. Fromme, N.A. Zatsepin, K.N. Rendek, M.S. Hunter, R.L. Shoeman, T.A. White, D. Wang, D. James, J.H. Yang, D.E. Cobb, B. Reeder, R.G. Sierra, H. Liu, A. Barty, A.L. Aquila, D. Deponte, R.A. Kirian, S. Bari, J.J. Bergkamp, K.R. Beyerlein, M.J. Bogan, C. Caleman, T.C. Chao, C.E. Conrad, K.M. Davis, H. Fleckenstein, L. Galli, S.P. Hau-Riege, S. Kassemeyer, H. Laksmono, M. Liang, L. Lomb, S. Marchesini, A.V. Martin, M. Messerschmidt, D. Milathianaki, K. Nass, A. Ros, S. Roy-Chowdhury, K. Schmidt, M. Seibert, J. Steinbrener, F. Stellato, L. Yan, C. Yoon, T.A. Moore, A.L. Moore, Y. Pushkar, G.J. Williams, S. Boutet, R.B. Doak, U. Weierstall, M. Frank, H.N. Chapman, J.C. Spence, P. Fromme, Serial time-resolved crystallography of photosystem II using a femtosecond X-ray laser, Nature 513 (2014) 261–265, https://doi.org/10.1038/nature13453.
[48] I.D. Young, M. Ibrahim, R. Chatterjee, S. Gul, F. Fuller, S. Koroidov, A.S. Brewster, R. Tran, R. Alonso-Mori, T. Kroll, T. Michels-Clark, H. Laksmono, R.G. Sierra, C.A. Stan, R. Hussein, M. Zhang, L. Douthit, M. Kubin, C. de Lichtenberg, P. Long Vo, H. Nilsson, M.H. Cheah, D. Shevela, C. Saracini, M.A. Bean, I. Seuffert, D. Sokaras, T.C. Weng, E. Pastor, C. Weninger, T. Fransson, L. Lassalle, P. Brauer, P. Aller, P.T. Docker, B. Andi, A.M. Orville, J.M. Glownia, S. Nelson, M. Sikorski, D. Zhu, M.S. Hunter, T.J. Lane, A. Aquila, J.E. Koglin, J. Robinson, M. Liang, S. Boutet, A.Y. Lyubimov, M. Uervirojnangkoorn, N.W. Moriarty, D. Liebschner, P.V. Afonine, D.G. Waterman, G. Evans, P. Wernet, H. Dobbek, W.I. Weis, A.T. Brunger, P.H. Zwart, P.D. Adams, A. Zouni, J. Messinger, U. Bergmann, N.K. Sauter, J. Kern, V.K. Yachandra, J. Yano, Structure of photosystem II and substrate binding at room temperature, Nature 540 (2016) 453–457, https://doi.org/10.1038/nature20161.
[49] Y. Kato, F. Akita, Y. Nakajima, M. Suga, Y. Umena, J.R. Shen, T. Noguchi, Fourier transform infrared analysis of the S-state cycle of water oxidation in the microcrystals of photosystem II, J. Phys. Chem. Lett. 9 (2018) 2121–2126, https://doi.org/10.1021/acs.jpclett.8b00638.
[50] K. Saito, A.W. Rutherford, H. Ishikita, Energetics of proton release on the first oxidation step in the water-oxidizing enzyme, Nat. Commun. 6 (2015) 8488, https://doi.org/10.1038/ncomms9488.
[51] H. Isobe, M. Shoji, J.R. Shen, K. Yamaguchi, Chemical equilibrium models for the S_3 state of the oxygen-evolving complex of photosystem II, Inorg. Chem. 55 (2016) 502–511, https://doi.org/10.1021/acs.inorgchem.5b02471.
[52] K. Kawakami, Y. Umena, N. Kamiya, J.R. Shen, Structure of the catalytic, inorganic core of oxygen-evolving photosystem II at 1.9 Å resolution, J. Photochem. Photobiol. B 104 (2011) 9–18, https://doi.org/10.1016/j.jphotobiol.2011.03.017.
[53] S. Yoshikawa, A. Shimada, Reaction mechanism of cytochrome *c* oxidase, Chem. Rev. 115 (2015), https://doi.org/10.1021/cr500266a.
[54] S. Yoshikawa, K. Muramoto, K. Shinzawa-Itoh, Proton-pumping mechanism of cytochrome *c* oxidase, Anu. Rev. Biophys. 40 (2011) 205–223, https://doi.org/10.1146/annurev-biophys-042910-155341.
[55] T. Tsukihara, H. Aoyama, E. Yamashita, T. Tomizaki, H. Yamaguchi, K. Shinzawa-Itoh, R. Nakashima, R. Yaono, S. Yoshikawa, Structures of metal sites of oxidized bovine heart cytochrome *c* oxidase at 2.8 Å, Science 269 (1995) 1069–1074 http://www.ncbi.nlm.nih.gov/pubmed/7652554.
[56] T. Tsukihara, K. Shimokata, Y. Katayama, H. Shimada, K. Muramoto, H. Aoyama, M. Mochizuki, K. Shinzawa-Itoh, E. Yamashita, M. Yao, Y. Ishimura, S. Yoshikawa, The low-spin heme of cytochrome *c* oxidase as the driving element of the proton-pumping process, Proc. Natl. Acad. Sci. U. S. A. 100 (2003) 15304–15309, https://doi.org/10.1073/pnas.2635097100.
[57] S. Yoshikawa, K. Shinzawa-Itoh, R. Nakashima, R. Yaono, E. Yamashita, N. Inoue, M. Yao, M.J. Fei, C.P. Libeu, T. Mizushima, H. Yamaguchi, T. Tomizaki, T. Tsukihara, Redox-coupled crystal structural changes in bovine heart cytochrome *c* oxidase, Science 280 (1998) 1723–1729, https://doi.org/10.1126/science.280.5370.1723.
[58] A.J. Moody, C.E. Cooper, P.R. Rich, Characterisation of 'fast' and 'slow' forms of bovine heart cytochrome-*c* oxidase, Biochim. Biophys. Acta 1059 (1991) 189–207, https://doi.org/10.1016/S0005-2728(05)80204-X.
[59] M. Mochizuki, H. Aoyama, K. Shinzawa-Itoh, T. Usui, T. Tsukihara, S. Yoshikawa, Quantitative reevaluation of the redox active sites of crystalline bovine heart cytochrome *c* oxidase, J. Biol. Chem. 274 (1999) 33403–33411 http://www.ncbi.nlm.nih.gov/pubmed/10559221.
[60] G.M. Baker, M. Noguchi, G. Palmer, The reaction of cytochrome oxidase with cyanide. Preparation of the rapidly reacting form and its conversion to the slowly reacting form, J. Biol. Chem. 262 (1987) 595–604 http://www.ncbi.nlm.nih.gov/pubmed/3027057.
[61] A. Sucheta, I. Szundi, O. Einarsdottir, Intermediates in the reaction of fully reduced cytochrome *c* oxidase with dioxygen, Biochemistry 37 (1998) 17905–17914, https://doi.org/10.1021/bi981092w.
[62] T. Ogura, S. Hirota, D.A. Proshlyakov, K. ShinzawaItoh, S. Yoshikawa, T. Kitagawa, Time-resolved resonance Raman evidence for tight coupling between electron transfer and proton pumping of cytochrome *c* oxidase upon the change from the Fe-V oxidation level to the Fe-IV oxidation level, J. Am. Chem. Soc. 118 (1996) 5443–5449, https://doi.org/10.1021/ja951922i.
[63] T. Ogura, S. Takahashi, S. Hirota, K. Shinzawaitoh, S. Yoshikawa, E.H. Appelman, T. Kitagawa, Time-resolved resonance Raman elucidation of the pathway for dioxygen reduction by cytochrome-*c*-oxidase, J. Am. Chem. Soc. 115 (1993) 8527–8536, https://doi.org/10.1021/ja00072a002.
[64] D.L. Rousseau, S. Han, Time-resolved resonance Raman spectroscopy of intermediates in cytochrome oxidase, Methods Enzymol. 354 (2002) 351–368, https://doi.org/10.1016/s0076-6879(02)54028-3.
[65] D. Bloch, I. Belevich, A. Jasaitis, C. Ribacka, A. Puustinen, M.I. Verkhovsky, M. Wikström, The catalytic cycle of cytochrome *c* oxidase is not the sum of its two halves, Proc. Natl. Acad. Sci. U. S. A. 101 (2004) 529–533, https://doi.org/10.1073/pnas.0306036101.
[66] K. Faxén, G. Gilderson, P. Adelroth, P. Brzezinski, A mechanistic principle for

proton pumping by cytochrome *c* oxidase, Nature 437 (2005) 286–289, https://doi.org/10.1038/nature03921.
[67] S.A. Siletsky, A.A. Konstantinov, Cytochrome *c* oxidase: charge translocation coupled to single-electron partial steps of the catalytic cycle, Biochim. Biophys. Acta 1817 (2012) 476–488, https://doi.org/10.1016/j.bbabio.2011.08.003.
[68] M.I. Verkhovsky, A. Jasaitis, M.L. Verkhovskaya, J.E. Morgan, M. Wikström, Proton translocation by cytochrome *c* oxidase, Nature 400 (1999) 480–483, https://doi.org/10.1038/22813.
[69] K. Muramoto, K. Ohta, K. Shinzawa-Itoh, K. Kanda, M. Taniguchi, H. Nabekura, E. Yamashita, T. Tsukihara, S. Yoshikawa, Bovine cytochrome *c* oxidase structures enable O_2 reduction with minimization of reactive oxygens and provide a proton-pumping gate, Proc. Natl. Acad. Sci. U. S. A. 107 (2010) 7740–7745, https://doi.org/10.1073/pnas.0910410107.
[70] R.B. Dyer, K.A. Peterson, P.O. Stoutland, W.H. Woodruff, Picosecond infrared study of the photodynamics of carbonmonoxy-cytochrome *c* oxidase, Biochemistry 33 (1994) 500–507, https://doi.org/10.1021/bi00168a015.
[71] O. Einarsdóttir, R.B. Dyer, D.D. Lemon, P.M. Killough, S.M. Hubig, S.J. Atherton, J.J. López-Garriga, G. Palmer, W.H. Woodruff, Photodissociation and recombination of carbonmonoxy cytochrome oxidase: dynamics from picoseconds to kiloseconds, Biochemistry 32 (1993) 12013–12024, https://doi.org/10.1021/bi00096a011.
[72] R.B. Gennis, Some recent contributions of FTIR difference spectroscopy to the study of cytochrome oxidase, FEBS Lett. 555 (2003) 2–7, https://doi.org/10.1016/s0014-5793(03)01150-5.
[73] M. Kubo, S. Nakashima, S. Yamaguchi, T. Ogura, M. Mochizuki, J. Kang, M. Tateno, K. Shinzawa-Itoh, K. Kato, S. Yoshikawa, Effective pumping proton collection facilitated by a copper site (Cu_B) of bovine heart cytochrome *c* oxidase, revealed by a newly developed time-resolved infrared system, J. Biol. Chem. 288 (2013) 30259–30269, https://doi.org/10.1074/jbc.M113.473983.
[74] N. Yano, K. Muramoto, A. Shimada, S. Takemura, J. Baba, H. Fujisawa, M. Mochizuki, K. Shinzawa-Itoh, E. Yamashita, T. Tsukihara, S. Yoshikawa, The Mg^{2+}-containing water cluster of mammalian cytochrome *c* oxidase collects four pumping proton equivalents in each catalytic cycle, J. Biol. Chem. 291 (2016) 23882–23894, https://doi.org/10.1074/jbc.M115.711770.
[75] J.O. Alben, P.P. Moh, F.G. Fiamingo, R.A. Altschuld, Cytochrome oxidase (a3) heme and copper observed by low-temperature Fourier transform infrared spectroscopy of the CO complex, Proc. Natl. Acad. Sci. U. S. A. 78 (1981) 234–237, https://doi.org/10.1073/pnas.78.1.234.
[76] S. Baba, T. Hoshino, L. Ito, T. Kumasaka, Humidity control and hydrophilic glue coating applied to mounted protein crystals improves X-ray diffraction experiments, Acta Crystallogr. D Biol. Crystallogr. 69 (2013) 1839–1849, https://doi.org/10.1107/S0907444913018027.
[77] W.H. Woodruff, O. Einarsdottir, R.B. Dyer, K.A. Bagley, G. Palmer, S.J. Atherton, R.A. Goldbeck, T.D. Dawes, D.S. Kliger, Nature and functional implications of the cytochrome a3 transients after photodissociation of CO-cytochrome oxidase, Proc. Natl. Acad. Sci. U. S. A. 88 (1991) 2588–2592, https://doi.org/10.1073/pnas.88.6.2588.
[78] W.G. Zumft, Cell biology and molecular basis of denitrification, Microbiol. Mol. Biol. Rev. 61 (1997) 533–616 https://www.ncbi.nlm.nih.gov/pubmed/9409151.
[79] S.J. Ferguson, Nitrogen cycle enzymology, Curr. Opin. Chem. Biol. 2 (1998) 182–193 https://www.ncbi.nlm.nih.gov/pubmed/9667932.
[80] D.J. Richardson, N.J. Watmough, Inorganic nitrogen metabolism in bacteria, Curr. Opin. Chem. Biol. 3 (1999) 207–219, https://doi.org/10.1016/S1367-5931(99)80034-9.
[81] S.A. Montzka, E.J. Dlugokencky, J.H. Butler, Non-CO_2 greenhouse gases and climate change, Nature 476 (2011) 43–50, https://doi.org/10.1038/nature10322.
[82] M.J. Prather, J. Hsu, Coupling of nitrous oxide and methane by global atmospheric chemistry, Science 330 (2010) 952–954, https://doi.org/10.1126/science.1196285.
[83] A.R. Ravishankara, J.S. Daniel, R.W. Portmann, Nitrous oxide (N_2O): the dominant ozone-depleting substance emitted in the 21st century, Science 326 (2009) 123–125, https://doi.org/10.1126/science.1176985.
[84] D. Kanter, D.L. Mauzerall, A.R. Ravishankara, J.S. Daniel, R.W. Portmann, P.M. Grabiel, W.R. Moomaw, J.N. Galloway, A post-Kyoto partner: considering the stratospheric ozone regime as a tool to manage nitrous oxide, Proc. Natl. Acad. Sci. U. S. A. 110 (2013) 4451–4457, https://doi.org/10.1073/pnas.1222231110.
[85] A.K. Jain, B.P. Briegleb, K. Minschwaner, D.J. Wuebbles, Radiative forcings and global warming potentials of 39 greenhouse gases, J. Geophys. Res.-Atmos. 105 (2000) 20773–20790, https://doi.org/10.1029/2000jd900241.
[86] G. Myhre, D. Shindell, F.o.-M. Bréon, W. Collins, J. Fuglestvedt, J. Huang, D. Koch, J.-F.O. Lamarque, D. Lee, B. Mendoza, T. Nakajima, A. Robock, G. Stephens, T. Takemura, H. Zhang, Anthropogenic and natural radiative forcing, in: T.F. Stocker, D. Qin, G.-K. Plattner, M. Tignor, S.K. Allen, J. Boschung, A. Nauels, Y. Xia, V. Bex, P.M. Midgley (Eds.), Climate Change 2013: The Physical Science Basis. Contribution of Working Group I to the Fifth Assessment Report of the Intergovernmental Panel on Climate Change, Cambridge University Press, Cambridge, United Kingdom and New York, NY, USA, 2013, pp. 659–740 https://www.ipcc.ch/site/assets/uploads/2018/02/WG1AR5_Chapter08_FINAL.pdf.
[87] D.S. Reay, E.A. Davidson, K.A. Smith, P. Smith, J.M. Melillo, F. Dentener, P.J. Crutzen, Global agriculture and nitrous oxide emissions, Nat. Clim. Chang. 2 (2012) 410–416, https://doi.org/10.1038/nclimate1458.
[88] H. Shoun, D.H. Kim, H. Uchiyama, J. Sugiyama, Denitrification by fungi, FEMS Microbiol. Lett. 73 (1992) 277–281, https://doi.org/10.1016/0378-1097(92)90643-3.
[89] S. Tsuruta, N. Takaya, L. Zhang, H. Shoun, K. Kimura, M. Hamamoto, T. Nakase, Denitrification by yeasts and occurrence of cytochrome P450nor in *Trichosporon cutaneum*, FEMS Microbiol. Lett. 168 (1998) 105–110, https://doi.org/10.1111/j.1574-6968.1998.tb13262.x.
[90] H. Shoun, T. Tanimoto, Denitrification by the fungus *Fusarium oxysporum* and involvement of cytochrome P-450 in the respiratory nitrite reduction, J. Biol. Chem. 266 (1991) 11078–11082 https://www.ncbi.nlm.nih.gov/pubmed/2040619.
[91] H. Shoun, S. Fushinobu, L. Jiang, S.W. Kim, T. Wakagi, Fungal denitrification and nitric oxide reductase cytochrome P450nor, Philos. Trans. R. Soc. Lond. Ser. B Biol. Sci. 367 (2012) 1186–1194, https://doi.org/10.1098/rstb.2011.0335.
[92] T. Hino, S. Nagano, H. Sugimoto, T. Tosha, Y. Shiro, Molecular structure and function of bacterial nitric oxide reductase, Biochim. Biophys. Acta 1817 (2012) 680–687, https://doi.org/10.1016/j.bbabio.2011.09.021.
[93] R. Oshima, S. Fushinobu, F. Su, L. Zhang, N. Takaya, H. Shoun, Structural evidence for direct hydride transfer from NADH to cytochrome P450nor, J. Mol. Biol. 342 (2004) 207–217, https://doi.org/10.1016/j.jmb.2004.07.009.
[94] T. Omura, Structural diversity of cytochrome P450 enzyme system, J. Biochem. 147 (2010) 297–306, https://doi.org/10.1093/jb/mvq001.
[95] E. Obayashi, S. Takahashi, Y. Shiro, Electronic structure of reaction intermediate of cytochrome P450nor in its nitric oxide reduction, J. Am. Chem. Soc. 120 (1998) 12964–12965, https://doi.org/10.1021/ja9813764.
[96] N. Okamoto, Y. Imai, H. Shoun, Y. Shiro, Site-directed mutagenesis of the conserved threonine (Thr243) of the distal helix of fungal cytochrome P450nor, Biochemistry 37 (1998) 8839–8847, https://doi.org/10.1021/bi980469v.
[97] Y. Shiro, M. Fujii, T. Iizuka, S. Adachi, K. Tsukamoto, K. Nakahara, H. Shoun, Spectroscopic and kinetic studies on reaction of cytochrome P450nor with nitric oxide. Implication for its nitric oxide reduction mechanism, J. Biol. Chem. 270 (1995) 1617–1623, https://doi.org/10.1074/jbc.270.4.1617.
[98] Y. Shiro, M. Fujii, Y. Isogai, S. Adachi, T. Iizuka, E. Obayashi, R. Makino, K. Nakahara, H. Shoun, Iron-ligand structure and iron redox property of nitric oxide reductase cytochrome P450nor from *Fusarium oxysporum*: relevance to its NO reduction activity, Biochemistry 34 (1995) 9052–9058 https://www.ncbi.nlm.nih.gov/pubmed/7619804.
[99] E.G. Abucayon, R.L. Khade, D.R. Powell, Y. Zhang, G.B. Richter-Addo, Hydride attack on a coordinated ferric nitrosyl: experimental and DFT evidence for the formation of a heme model-HNO derivative, J. Am. Chem. Soc. 138 (2016) 104–107, https://doi.org/10.1021/jacs.5b12008.
[100] L.E. Goodrich, F. Paulat, V.K. Praneeth, N. Lehnert, Electronic structure of heme-nitrosyls and its significance for nitric oxide reactivity, sensing, transport, and toxicity in biological systems, Inorg. Chem. 49 (2010) 6293–6316, https://doi.org/10.1021/ic902304a.
[101] B. Kramos, D.K. Menyhard, J. Olah, Direct hydride shift mechanism and stereoselectivity of P450nor confirmed by QM/MM calculations, J. Phys. Chem. B 116 (2012) 872–885, https://doi.org/10.1021/jp2080918.
[102] C. Riplinger, E. Bill, A. Daiber, V. Ullrich, H. Shoun, F. Neese, New insights into the nature of observable reaction intermediates in cytochrome P450 NO reductase by using a combination of spectroscopy and quantum mechanics/molecular mechanics calculations, Chemistry 20 (2014) 1602–1614, https://doi.org/10.1002/chem.201302443.
[103] S.Y. Park, H. Shimizu, S. Adachi, A. Nakagawa, I. Tanaka, K. Nakahara, H. Shoun, E. Obayashi, H. Nakamura, T. Iizuka, Y. Shiro, Crystal structure of nitric oxide reductase from denitrifying fungus fusarium oxysporum, Nat. Struct. Biol. 4 (1997) 827–832 https://www.ncbi.nlm.nih.gov/pubmed/9334748.
[104] H. Shimizu, S. Park, D. Lee, H. Shoun, Y. Shiro, Crystal structures of cytochrome P450nor and its mutants (Ser286– > Val, Thr) in the ferric resting state at cryogenic temperature: a comparative analysis with monooxygenase cytochrome P450s, J. Inorg. Biochem. 81 (2000) 191–205 https://www.ncbi.nlm.nih.gov/pubmed/11051564.
[105] T.R. Barends, L. Foucar, A. Ardevol, K. Nass, A. Aquila, S. Botha, R.B. Doak, K. Falahati, E. Hartmann, M. Hilpert, M. Heinz, M.C. Hoffmann, J. Kofinger, J.E. Koglin, G. Kovacsova, M. Liang, D. Milathianaki, H.T. Lemke, J. Reinstein, C.M. Roome, R.L. Shoeman, G.J. Williams, I. Burghardt, G. Hummer, S. Boutet, I. Schlichting, Direct observation of ultrafast collective motions in CO myoglobin upon ligand dissociation, Science 350 (2015) 445–450, https://doi.org/10.1126/science.aac5492.
[106] J. Tenboer, S. Basu, N. Zatsepin, K. Pande, D. Milathianaki, M. Frank, M. Hunter, S. Boutet, G.J. Williams, J.E. Koglin, D. Oberthuer, M. Heymann, C. Kupitz, C. Conrad, J. Coe, S. Roy-Chowdhury, U. Weierstall, D. James, D. Wang, T. Grant, A. Barty, O. Yefanov, J. Scales, C. Gati, C. Seuring, V. Srajer, R. Henning, P. Schwander, R. Fromme, A. Ourmazd, K. Moffat, J.J. Van Thor, J.C. Spence, P. Fromme, H.N. Chapman, M. Schmidt, Time-resolved serial crystallography captures high-resolution intermediates of photoactive yellow protein, Science 346 (2014) 1242–1246, https://doi.org/10.1126/science.1259357.
[107] P. Nogly, T. Weinert, D. James, S. Carbajo, D. Ozerov, A. Furrer, D. Gashi, V. Borin, P. Skopintsev, K. Jaeger, K. Nass, P. Bath, R. Bosman, J. Koglin, M. Seaberg, T. Lane, D. Kekilli, S. Brunle, T. Tanaka, W. Wu, C. Milne, T. White, A. Barty, U. Weierstall, V. Panneels, E. Nango, S. Iwata, M. Hunter, I. Schapiro, G. Schertler, R. Neutze, J. Standfuss, Retinal isomerization in bacteriorhodopsin captured by a femtosecond x-ray laser, Science 361 (2018), https://doi.org/10.1126/science.aat0094.
[108] C. Wickstrand, P. Nogly, E. Nango, S. Iwata, J. Standfuss, R. Neutze, Bacteriorhodopsin: structural insights revealed using X-ray lasers and synchrotron radiation, Annu. Rev. Biochem. (2019), https://doi.org/10.1146/annurev-biochem-013118-111327.
[109] I. Schlichting, S.C. Almo, G. Rapp, K. Wilson, K. Petratos, A. Lentfer, A. Wittinghofer, W. Kabsch, E.F. Pai, G.A. Petsko, et al., Time-resolved X-ray crystallographic study of the conformational change in ha-Ras p21 protein on GTP

hydrolysis, Nature 345 (1990) 309–315, https://doi.org/10.1038/345309a0.
[110] S. Namiki, T. Arai, K. Fujimori, High-performance caged nitric oxide: a new molecular design, synthesis, and photochemical reaction, J. Am. Chem. Soc. 119 (1997) 3840–3841, https://doi.org/10.1021/ja962839d.
[111] M. Sugahara, T. Nakane, T. Masuda, M. Suzuki, S. Inoue, C. Song, R. Tanaka, T. Nakatsu, E. Mizohata, F. Yumoto, K. Tono, Y. Joti, T. Kameshima, T. Hatsui, M. Yabashi, O. Nureki, K. Numata, E. Nango, S. Iwata, Hydroxyethyl cellulose matrix applied to serial crystallography, Sci. Rep. 7 (2017) 703, https://doi.org/10.1038/s41598-017-00761-0.
[112] J.R. Stagno, Y. Liu, Y.R. Bhandari, C.E. Conrad, S. Panja, M. Swain, L. Fan, G. Nelson, C. Li, D.R. Wendel, T.A. White, J.D. Coe, M.O. Wiedorn, J. Knoska, D. Oberthuer, R.A. Tuckey, P. Yu, M. Dyba, S.G. Tarasov, U. Weierstall, T.D. Grant, C.D. Schwieters, J. Zhang, A.R. Ferre-D'Amare, P. Fromme, D.E. Draper, M. Liang, M.S. Hunter, S. Boutet, K. Tan, X. Zuo, X. Ji, A. Barty, N.A. Zatsepin, H.N. Chapman, J.C. Spence, S.A. Woodson, Y.X. Wang, Structures of riboswitch RNA reaction states by mix-and-inject XFEL serial crystallography, Nature 541 (2017) 242–246, https://doi.org/10.1038/nature20599.
[113] F.D. Fuller, S. Gul, R. Chatterjee, E.S. Burgie, I.D. Young, H. Lebrette, V. Srinivas, A.S. Brewster, T. Michels-Clark, J.A. Clinger, B. Andi, M. Ibrahim, E. Pastor, C. de Lichtenberg, R. Hussein, C.J. Pollock, M. Zhang, C.A. Stan, T. Kroll, T. Fransson, C. Weninger, M. Kubin, P. Aller, L. Lassalle, P. Brauer, M.D. Miller, M. Amin, S. Koroidov, C.G. Roessler, M. Allaire, R.G. Sierra, P.T. Docker, J.M. Glownia, S. Nelson, J.E. Koglin, D. Zhu, M. Chollet, S. Song, H. Lemke, M. Liang, D. Sokaras, R. Alonso-Mori, A. Zouni, J. Messinger, U. Bergmann, A.K. Boal, J.M. Bollinger Jr., C. Krebs, M. Hogbom, G.N. Phillips Jr., R.D. Vierstra, N.K. Sauter, A.M. Orville, J. Kern, V.K. Yachandra, J. Yano, Drop-on-demand sample delivery for studying biocatalysts in action at X-ray free-electron lasers, Nat. Methods 14 (2017) 443–449, https://doi.org/10.1038/nmeth.4195.
[114] C.G. Roessler, R. Agarwal, M. Allaire, R. Alonso-Mori, B. Andi, J.F.R. Bachega, M. Bommer, A.S. Brewster, M.C. Browne, R. Chatterjee, E. Cho, A.E. Cohen, M. Cowan, S. Datwani, V.L. Davidson, J. Defever, B. Eaton, R. Ellson, Y. Feng, L.P. Ghislain, J.M. Glownia, G. Han, J. Hattne, J. Hellmich, A. Heroux, M. Ibrahim, J. Kern, A. Kuczewski, H.T. Lemke, P. Liu, L. Majlof, W.M. McClintock, S. Myers, S. Nelsen, J. Olechno, A.M. Orville, N.K. Sauter, A.S. Soares, S.M. Soltis, H. Song, R.G. Stearns, R. Tran, Y. Tsai, M. Uervirojnangkoorn, C.M. Wilmot, V. Yachandra, J. Yano, E.T. Yukl, D. Zhu, A. Zouni, Acoustic injectors for drop-on-demand serial femtosecond crystallography, Structure 24 (2016) 631–640, https://doi.org/10.1016/j.str.2016.02.007.
[115] A. Ebrahim, M.V. Appleby, D. Axford, J. Beale, T. Moreno-Chicano, D.A. Sherrell, R.W. Strange, M.A. Hough, R.L. Owen, Resolving polymorphs and radiation-driven effects in microcrystals using fixed-target serial synchrotron crystallography, Acta Crystallogr. D Biol. Crystallogr. 75 (2019) 151–159, https://doi.org/10.1107/S2059798318010240.
[116] D.P. DePonte, U. Weierstall, K. Schmidt, J. Warner, D. Starodub, J.C.H. Spence, R.B. Doak, Gas dynamic virtual nozzle for generation of microscopic droplet streams, J. Phys. D Appl. Phys. 41 (2008), https://doi.org/10.1088/0022-3727/41/19/195505.
[117] C. Song, K. Tono, J. Park, T. Ebisu, S. Kim, H. Shimada, S. Kim, M. Gallagher-Jones, D. Nam, T. Sato, T. Togashi, K. Ogawa, Y. Joti, T. Kameshima, S. Ono, T. Hatsui, S. Iwata, M. Yabashi, T. Ishikawa, Multiple application X-ray imaging chamber for single-shot diffraction experiments with femtosecond X-ray laser pulses, J. Appl. Crystallogr. 47 (2014) 188–197, https://doi.org/10.1107/S1600576713029944.
[118] D. James, T. Weinert, P. Skopintsev, A. Furrer, D. Gashi, T. Tanaka, E. Nango, P. Nogly, J. Standfuss, Improving high viscosity extrusion of microcrystals for time-resolved serial femtosecond crystallography at X-ray lasers, J. Vis. Exp. (2019), https://doi.org/10.3791/59087.
[119] L.C. Johansson, D. Arnlund, T.A. White, G. Katona, D.P. Deponte, U. Weierstall, R.B. Doak, R.L. Shoeman, L. Lomb, E. Malmerberg, J. Davidsson, K. Nass, M. Liang, J. Andreasson, A. Aquila, S. Bajt, M. Barthelmess, A. Barty, M.J. Bogan, C. Bostedt, J.D. Bozek, C. Caleman, R. Coffee, N. Coppola, T. Ekeberg, S.W. Epp, B. Erk, H. Fleckenstein, L. Foucar, H. Graafsma, L. Gumprecht, J. Hajdu, C.Y. Hampton, R. Hartmann, A. Hartmann, G. Hauser, H. Hirsemann, P. Holl, M.S. Hunter, S. Kassemeyer, N. Kimmel, R.A. Kirian, F.R. Maia, S. Marchesini, A.V. Martin, C. Reich, D. Rolles, B. Rudek, A. Rudenko, I. Schlichting, J. Schulz, M.M. Seibert, R.G. Sierra, H. Soltau, D. Starodub, F. Stellato, S. Stern, L. Struder, N. Timneanu, J. Ullrich, W.Y. Wahlgren, X. Wang, G. Weidenspointner, C. Wunderer, P. Fromme, H.N. Chapman, J.C. Spence, R. Neutze, Lipidic phase membrane protein serial femtosecond crystallography, Nat. Methods 9 (2012) 263–265, https://doi.org/10.1038/nmeth.1867.
[120] P. Nogly, V. Panneels, G. Nelson, C. Gati, T. Kimura, C. Milne, D. Milathianaki, M. Kubo, W. Wu, C. Conrad, J. Coe, R. Bean, Y. Zhao, P. Bath, R. Dods, R. Harimoorthy, K.R. Beyerlein, J. Rheinberger, D. James, D. DePonte, C. Li, L. Sala, G.J. Williams, M.S. Hunter, J.E. Koglin, P. Berntsen, E. Nango, S. Iwata, H.N. Chapman, P. Fromme, M. Frank, R. Abela, S. Boutet, A. Barty, T.A. White, U. Weierstall, J. Spence, R. Neutze, G. Schertler, J. Standfuss, Lipidic cubic phase injector is a viable crystal delivery system for time-resolved serial crystallography, Nat. Commun. 7 (2016) 12314, , https://doi.org/10.1038/ncomms12314.
[121] U. Weierstall, D. James, C. Wang, T.A. White, D. Wang, W. Liu, J.C. Spence, R. Bruce Doak, G. Nelson, P. Fromme, R. Fromme, I. Grotjohann, C. Kupitz, N.A. Zatsepin, H. Liu, S. Basu, D. Wacker, G.W. Han, V. Katritch, S. Boutet, M. Messerschmidt, G.J. Williams, J.E. Koglin, M. Marvin Seibert, M. Klinker, C. Gati, R.L. Shoeman, A. Barty, H.N. Chapman, R.A. Kirian, K.R. Beyerlein, R.C. Stevens, D. Li, S.T. Shah, N. Howe, M. Caffrey, V. Cherezov, Lipidic cubic phase injector facilitates membrane protein serial femtosecond crystallography, Nat. Commun. 5 (2014) 3309, https://doi.org/10.1038/ncomms4309.
[122] C. Mueller, A. Marx, S.W. Epp, Y. Zhong, A. Kuo, A.R. Balo, J. Soman, F. Schotte, H.T. Lemke, R.L. Owen, E.F. Pai, A.R. Pearson, J.S. Olson, P.A. Anfinrud, O.P. Ernst, R.J. Dwayne Miller, Fixed target matrix for femtosecond time-resolved and in situ serial micro-crystallography, Struct. Dyn. 2 (2015) 054302, , https://doi.org/10.1063/1.4928706.
[123] M.L. Grunbein, G.N. Kovacs, Sample delivery for serial crystallography at free-electron lasers and synchrotrons, Acta Crystallogr. D Biol. Crystallogr. 75 (2019) 178–191, https://doi.org/10.1107/S205979831801567x.
[124] J. Standfuss, Membrane protein dynamics studied by X-ray lasers - or why only time will tell, Curr. Opin. Struct. Biol. 57 (2019) 63–71, https://doi.org/10.1016/j.sbi.2019.02.001.
[125] G.K. Feld, M. Frank, Enabling membrane protein structure and dynamics with X-ray free electron lasers, Curr. Opin. Struct. Biol. 27 (2014) 69–78, https://doi.org/10.1016/j.sbi.2014.05.002.
[126] I. Schlichting, R.S. Goody, Triggering methods in crystallographic enzyme kinetics, Methods Enzymol. 277 (1997) 467–490 https://www.ncbi.nlm.nih.gov/pubmed/18488320.
[127] I. Ishigami, A. Lewis-Ballester, A. Echelmeier, G. Brehm, N.A. Zatsepin, T.D. Grant, J.D. Coe, S. Lisova, G. Nelson, S. Zhang, Z.F. Dobson, S. Boutet, R.G. Sierra, A. Batyuk, P. Fromme, R. Fromme, J.C.H. Spence, A. Ros, S.R. Yeh, D.L. Rousseau, Snapshot of an oxygen intermediate in the catalytic reaction of cytochrome *c* oxidase, Proc. Natl. Acad. Sci. U. S. A. 116 (2019) 3572–3577, https://doi.org/10.1073/pnas.1814526116.
[128] G.C. Ellis-Davies, Caged compounds: photorelease technology for control of cellular chemistry and physiology, Nat. Methods 4 (2007) 619–628, https://doi.org/10.1038/nmeth1072.
[129] J.P. Kao, Caged molecules: principles and practical considerations, Curr. Protoc. Neurosci., Chapter 6 (2006) Unit 6 20, doi:https://doi.org/10.1002/0471142301.ns0620s37
[130] U. Alexiev, D.L. Farrens, Fluorescence spectroscopy of rhodopsins: insights and approaches, Biochim. Biophys. Acta 1837 (2014) 694–709, https://doi.org/10.1016/j.bbabio.2013.10.008.
[131] S.E. Mansoor, M.A. Dewitt, D.L. Farrens, Distance mapping in proteins using fluorescence spectroscopy: the tryptophan-induced quenching (TrIQ) method, Biochemistry 49 (2010) 9722–9731, https://doi.org/10.1021/bi100907m.